

See discussions, stats, and author profiles for this publication at: <https://www.researchgate.net/publication/7396702>

Ultrathin TiO(x) films on Pt(111): a LEED, XPS, and STM investigation.

ARTICLE in THE JOURNAL OF PHYSICAL CHEMISTRY B · JANUARY 2006

Impact Factor: 3.3 · DOI: 10.1021/jp0543173 · Source: PubMed

CITATIONS

100

READS

69

10 AUTHORS, INCLUDING:



Xesc Llabres

Spanish National Research Council

58 PUBLICATIONS 3,599 CITATIONS

SEE PROFILE



Anthoula C Papageorgiou

Technische Universität München

29 PUBLICATIONS 658 CITATIONS

SEE PROFILE



Klaus Schierbaum

Heinrich-Heine-Universität Düsseldorf

91 PUBLICATIONS 3,672 CITATIONS

SEE PROFILE



Gaetano Granozzi

University of Padova

301 PUBLICATIONS 4,395 CITATIONS

SEE PROFILE

Ultrathin TiO_x Films on Pt(111): A LEED, XPS, and STM Investigation

Francesco Sedona,[†] Gian Andrea Rizzi,[†] Stefano Agnoli,[†] Francesc X. Llabrés i Xamena,^{†,§} Anthoula Papageorgiou,^{†,||} Dieter Ostermann,[‡] Mauro Sambi,[†] Paola Finetti,[†] Klaus Schierbaum,[‡] and Gaetano Granozzi^{*,†}

Dipartimento di Scienze Chimiche and Unità di Ricerca INFM-CNR, Università di Padova, Via Marzolo, I-35131 Padova (Italy), and Institut für Physik der kondensierten Materie, Heinrich-Heine Universität Düsseldorf, Universitätsstrasse 1, D-40225 Düsseldorf (Germany)

Received: August 4, 2005; In Final Form: October 29, 2005

Ultrathin ordered titanium oxide films on Pt(111) surface are prepared by reactive evaporation of Ti in oxygen. By varying the Ti dose and the annealing conditions (i.e., temperature and oxygen pressure), six different long-range ordered phases are obtained. They are characterized by means of low-energy electron diffraction (LEED), X-ray photoemission spectroscopy (XPS), and scanning tunneling microscopy (STM). By careful optimization of the preparative parameters, we find conditions where predominantly single phases of TiO_x, revealing distinct LEED pattern and STM images, are produced. XPS binding energy and photoelectron diffraction (XPD) data indicate that all the phases, except one (the stoichiometric *rect*-TiO₂), are one monolayer thick and composed of a Ti–O bilayer with interfacial Ti. Atomically resolved STM images confirm that these TiO_x phases wet the Pt surface, in contrast to *rect*-TiO₂. This indicates their interface stabilization. At a low Ti dose (0.4 monolayer equivalents, MLE), an incommensurate kagomé-like low-density phase (*k*-TiO_x phase) is observed where hexagons are sharing their vertexes. At a higher Ti dose (0.8 MLE), two denser phases are found, both characterized by a zigzag motif (*z*- and *z'*-TiO_x phases), but with distinct rectangular unit cells. Among them, *z'*-TiO_x, which is obtained by annealing in ultrahigh vacuum (UHV), shows a larger unit cell. When the postannealing of the 0.8 MLE deposit is carried out at high temperatures and high oxygen partial pressures, the incommensurate nonwetting, fully oxidized *rect*-TiO₂ is found. The symmetry and lattice dimensions are almost identical with *rect*-VO₂, observed in the system VO_x/Pd(111). At a higher coverage (1.2 MLE), two commensurate hexagonal phases are formed, namely the *w*-[($\sqrt{43} \times \sqrt{43}$) *R* 7.6°] and *w'*-TiO_x phase [(7 × 7) *R* 21.8°]. They show wagon-wheel-like structures and have slightly different lattice dimensions. Larger Ti deposits produce TiO₂ nanoclusters on top of the different monolayer films, as supported both by XPS and STM data. Besides the formation of TiO_x surface phases, wormlike features are found on the bare parts of the substrate by STM. We suggest that these structures, probably multilayer disordered TiO₂, represent growth precursors of the ordered phases. Our results on the different nanostructures are compared with literature data on similar systems, e.g., VO_x/Pd(111), VO_x/Rh(111), TiO_x/Pd(111), TiO_x/Pt(111), and TiO_x/Ru(0001). Similar and distinct features are observed in the TiO_x/Pt(111) case, which may be related to the different chemical natures of the overlayer and of the substrate.

1. Introduction

Ultrathin ordered oxide films grown on single-crystal surfaces of metals are a topic of much interest in surface science. The term *ultrathin* relates to the extremely small thickness in the range up to one nanometer (i.e., in the monolayer, ML, range). The dimensional confinement, together with the interplay with the substrate, may lead to novel oxide structures, which are unknown in the bulk solid state. The vanadium oxide on Pd(111) and Rh(111) systems represent examples for which a variety of different surface-stabilized structures exist. They have been imaged with STM at atomic resolution, complemented by theoretical STM simulations and further surface spectroscopic techniques.^{1–6} Moreover, recent interest arises from the use of

ordered oxide layers as templates for epitaxial growth of other oxides and for the deposition of nanosized metal clusters. Specifically, the observed superstructure of an ultrathin alumina film grown on a Ni₃Al(111) crystal turns out to be an excellent template for the growth of palladium clusters forming a nanostructured array.⁷ Apart from the scientific challenges, unusual properties are anticipated for ultrathin ordered metal oxide films with implications to various fields of technological interest. On the other hand, well-ordered oxide films may have some relevance in order to tailor novel chemical sensors, e.g., field-effect and metal-oxide-semiconductor sensors.

Titanium oxide is certainly one of the best-characterized model systems in surface science.⁸ Most of the studies were performed on single-crystal surfaces, and only a few reports are addressed to ultrathin film investigations. Among these, Boffa et al. have reported an X-ray photoemission spectroscopy (XPS), low-energy electron diffraction (LEED) and scanning tunneling microscopy (STM) study on TiO_x grown on the Pt(111) surface.⁹ They describe a stoichiometric TiO₂ layer with

* gaetano.granozzi@unipd.it.

[†] Università di Padova.

[‡] Heinrich-Heine Universität Düsseldorf.

[§] Present address: Departamento de Química and Instituto de Tecnología Química, Universidad Politécnica de Valencia (Spain).

^{||} Permanent address: London Centre for Nanotechnology & Chemistry Department, University College London.

a hexagonal ($\sqrt{43} \times \sqrt{43}$) R 7.6° superstructure which corresponds to a unit cell of $18.2 \times 18.2 \text{ \AA}^2$. By heating to high temperature (923–1123 K) in ultrahigh vacuum (UHV), a second phase was observed with a stoichiometry close to Ti_4O_7 , exhibiting a superstructure with a size of $13.9 \times 18.2 \text{ \AA}^2$, noted as

$$\begin{bmatrix} 5 & 0 \\ 1 & 7 \end{bmatrix}$$

However, the quality of the STM images were not sufficient to derive the atomic structure of the corresponding film. Only a simplified structural model of the TiO_2 layer, derived from the (111) surface of rutile with significantly expanded O–O spacing, was proposed. For the Ti_4O_7 phase, a close relationship with the (100) surface of rutile and an ordered array of O defects was suggested.

Studies by Matsumoto et al. on TiO_x overlayers on Pt(100) have shown various oxide structures.^{10,11} Very recently, a detailed STM, XPS, and AES investigation on the growth and structures of ultrathin TiO_x films (from sub-monolayer to 1.5 ML range) on Ru(0001) has been reported by Männig et al.¹² They find different structures of Ti oxide, depending on coverage and postannealing conditions. The 1 ML $\text{TiO}_x/\text{Ru}(0001)$ film shows a ($6\sqrt{3} \times 6\sqrt{3}$)-like structure and a Moiré pattern in STM when quickly annealed at 1000 K in 10^{-5} Pa oxygen. They propose a structural model which is based on three stacked hexagonal layers O–Ti–O with an octahedral coordination of Ti by O ions.

An interesting relationship can be drawn between ultrathin titanium oxide layers and the encapsulation effect of Pt/ TiO_2 -(110). This encapsulation process has been related to the strong metal–support interaction (SMSI) effect, whose nature has been recently revisited.¹³ When TiO_2 (110) single crystal with Pt islands deposited on it is heated in UHV at 1100 K, one observes that the islands are covered with a very thin titanium oxide layer.¹⁴ Dulub et al. report atomically resolved STM images of such TiO_x overlayers where a zigzag-like motif is observed, and a structural model of the interface was proposed, supported by density functional theory (DFT) calculations.¹⁵ A similar encapsulation effect has been reported by Bennet et al. for Pd islands grown on TiO_2 (110) (1×2) upon heating at 973 K,¹⁶ and the results have been recently rediscussed.¹³ In this case, the imaged nanostructures exhibit typical zigzag-like or wagon-wheel habits.

In this paper, we report the results obtained for six different phases of TiO_x on the Pt(111) surface, prepared at coverages between 0.4 and 1.2 equivalent monolayers (MLE, see Experimental Section for its definition) by adopting a reactive evaporation of Ti at low O_2 pressures. The TiO_x phases are characterized by means of XPS, LEED, and STM. Preliminary photoelectron diffraction (XPD) data will be also presented for selected TiO_x phases. Particular emphasis is placed on elucidating the effects of initial Ti coverages and postannealing processes with the aim of finding experimental conditions suitable to grow single phases of titania on Pt(111) surfaces. The LEED patterns and STM images are herein compared with those of similar systems.

2. Experimental Section

The Pt(111) surface is prepared by several Ar^+ sputtering and annealing cycles at 870 K until the C 1s signal is below the detection limit of XPS. The subsequent inspection with LEED shows a clear (1×1) diffraction pattern. The deposition

of titania is performed in an oxygen background by electron-beam evaporation from a Ti wire. The TiO_x phases herein reported are prepared by varying the amount of the deposited Ti, given in MLE, where 1 MLE corresponds to $1.5 \cdot 10^{15}$ atoms cm^{-2} , as determined with a quartz microbalance. This number corresponds to the surface density of Pt atoms per unit area of Pt(111) $1 \times 1 \text{ (cm}^2 \text{ units)}$. For our experiments, we have chosen a deposition rate of 0.2 MLE per minute. Practically, we used different deposition times at a constant evaporation rate. The samples were then subjected to different annealing treatments, by heating them in UHV or in an oxygen background pressure in order to induce a structural ordering. Annealing in UHV produces a reduction of the oxide overlayer, while oxygen treatment causes oxidation. We noticed the tendency of Ti to dissolve into the substrate at high temperature, thereby forming a bulk alloy between Ti and Pt. On the other hand, samples with dissolved Ti exhibit a surface segregation of Ti during annealing in oxygen, thus yielding oxide overlayers. The temperature at which interdiffusion becomes significant depends strongly on the oxygen pressure. We experienced that the annealing temperature must be carefully adjusted in order to reduce the dissolution to a minimum and to avoid errors in the determination of the TiO_x coverages from the deposition time.

The preparation and XPS and LEED characterization of the films have been carried out in two different custom-made UHV chambers, both equipped with a sputter gun, an electron beam evaporator, a four-grid LEED optics, a hemispherical energy analyzer, and an X-ray double anode source. The XPS data reported in the present study were obtained using an Al $K\alpha$ radiation and with a pass energy of 20 eV. Binding energies (BEs) are referenced to the Pt $4f_{7/2}$ photoemission peak. In one of the two chambers, the sample is mounted on a two-axis goniometer, which allows us to rotate the sample in polar angle θ (with respect to the surface normal) and in azimuthal angle ϕ , so allowing collection of angle-scanned XPD data. Angular accuracy is always better than $\pm 1^\circ$ in both directions. The Ti 2p and O 1s XPD data reported herein are acquired for azimuthal scans at different polar angles with angular steps of 3° .

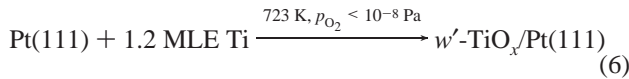
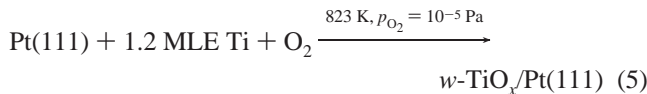
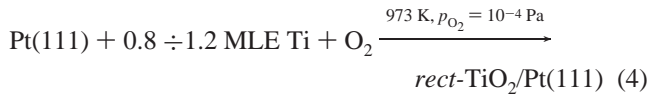
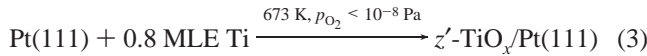
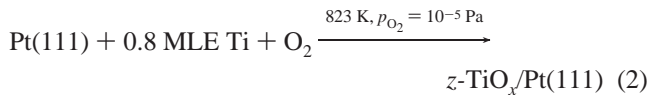
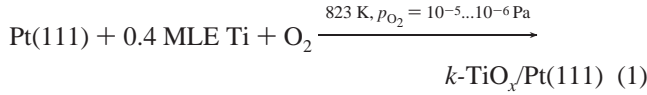
The STM images are taken at room temperature (RT) in an Omicron VT-STM system operating at a base pressure of 5×10^{-9} Pa. The system is equipped with a four-grid LEED optics. Pt–Ir tips were used in all the experiments. Tunneling voltages are given with respect to the sample. The tunneling parameters are reported in the corresponding captions of the reported STM images. The scanner was calibrated in the z -direction with respect to the step edge of the clean Pt(111) surface. For the lateral calibration, a (2×1) reconstructed Pt(110) surface has been used.

3. Results and Discussion

3.1. Preparation of TiO_x Films. Similar to other ultrathin oxides grown on single-crystal metal surfaces, we find different long-range ordered TiO_x phases as a function of the initial Ti dose and of the postannealing conditions. The initial Ti coverages that we have chosen to grow TiO_x on Pt(111) are 0.4, 0.8, and 1.2 MLE. All phases were prepared by reactive evaporation of Ti onto clean, freshly sputtered and annealed platinum single crystals, which are kept at room temperature (RT), in the presence of oxygen ($p_{\text{O}_2} = 10^{-4}$ Pa). The samples are then heated at elevated temperature T_{anneal} either in oxygen (at the same or lower p_{O_2} pressure) or in UHV (i.e., $p_{\text{O}_2} < 10^{-8}$ Pa), to improve the order of the films. Finally, the samples are cooled to RT and then characterized by XPS, LEED, and STM.

The annealing conditions as well as the Ti coverages have been varied with the aim of obtaining single phases of TiO_x with no significant contribution from other phases. This goal has been tested by LEED and checked by STM. Table 1 summarizes the six observed long-range ordered TiO_x phases on Pt(111). Figure 1 shows the LEED patterns, all taken at almost the same primary energies. In the table, the different phases are categorized according to the oxygen pressure of the annealing procedure and the nominal coverage in MLE. According to the LEED data, they show commensurate or incommensurate as well as hexagonal or rectangular surface unit cells. The observed superstructures are given in Table 1, adopting the matrix notation and, if applicable, the Wood notation. To provide the reader with a simple scheme of notation, phases that are known from previous reports on similar systems are named in a similar fashion. They are designated by different prefixes according to their characteristic STM appearance (z = zigzag-like, w = wagon-wheel-like, k = kagomé-like), as commonly used for such nanostructures. We find two wagon-wheel-like TiO_x phases with different commensurate hexagonal surface meshes, which are identified here as w and w' for the sake of simplification. Similarly, we find two zigzag-like phases: the incommensurate rectangular phase is denoted z -TiO_x, while for the commensurate $(6 \times 3\sqrt{3})$ -rect phase, we use z' -TiO_x. The rectangular TiO_x phase, whose LEED diffraction pattern and STM appearance show a close similarity to the literature *rect*-VO₂/Pd(111)²⁻⁴ is correspondingly labeled *rect*-TiO₂. At the low coverage of 0.4 MLE, an incommensurate hexagonal (2.15×2.15) phase appears which is called k -TiO_x, indicating the presence of a kagomé-like structure as seen by STM. The kagomé lattice is well-known by the experts of solid-state magnetism for its relevance in the emerging field of spintronics.^{17,18}

If p_{O_2} denotes the O₂ pressure, the formation of the TiO_x phases may be described by



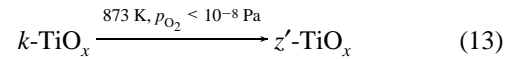
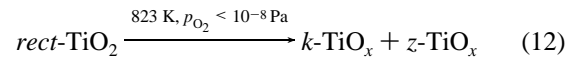
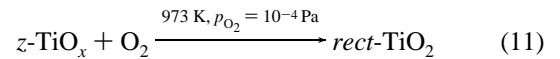
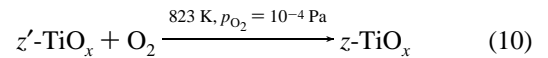
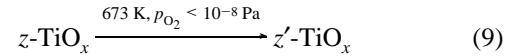
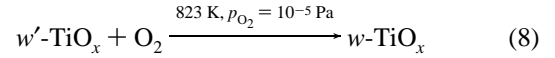
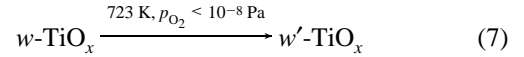
In these equations, the reported T_{anneal} represents the maximum value in order to avoid a detectable Ti interdiffusion into the substrate, and the MLE values are the nominal ones without any correction for minor changes to be associated to possible interdiffusion.

TABLE 1: Summary of the Titanium Oxide Phases on Pt(111) Described in This Work^e

annealing O ₂ pressure (Pa)	10 ⁻⁴	<i>rect</i> -TiO ₂ ^{a)} $\begin{bmatrix} 1.16 & 0.18 \\ 0.58 & 1.56 \end{bmatrix}$ incommensurate rectangular		
	10 ⁻⁵	<i>k</i> -TiO _x ^{a)} $\begin{bmatrix} 2.15 & 0 \\ 0 & 2.15 \end{bmatrix}$ incommensurate hexagonal	<i>z</i> -TiO _x ^{b)} $\begin{bmatrix} 2.5 & 0 \\ 1.8 & 3.6 \end{bmatrix}$ incommensurate rectangular	<i>w</i> -TiO _x ^{c)} $\begin{bmatrix} 7 & 1 \\ -1 & 6 \end{bmatrix}$ ($\sqrt{43} \times \sqrt{43}$)R7.6° commensurate hexagonal
	<10 ⁻⁸ (UHV)		<i>z'</i> -TiO _x ^{b)} $\begin{bmatrix} 6 & 0 \\ 3 & 6 \end{bmatrix}$ (6×3 $\sqrt{3}$)-Rect commensurate rectangular	<i>w'</i> -TiO _x ^{c)} $\begin{bmatrix} 8 & 3 \\ -3 & 5 \end{bmatrix}$ (7 × 7)R21.8° commensurate hexagonal
		0.4	0.8	1.2
	equivalent monolayer (MLE)			

^a k = kagomé. ^b z = zigzag-like. ^c w = wagon-wheel-like. ^d *rect* = rectangular. ^e Superstructures in matrix notation are related to the hexagonal mesh of Pt(111) with $d = 2.77 \text{ \AA}$ and $\alpha = 120^\circ$.

In addition to these routes toward TiO_x phases, the following structural transformations of the films occur upon subsequent sample treatments:



Reactions 7 and 8 concern the reversible transformation of the two wagon-wheel-like TiO_x phases, obviously as a result of reduction and oxidation of the film. The z -TiO_x phase can be reduced to z' -TiO_x in UHV (reaction 9) (this reaction can be reversed by oxygen annealing, reaction 10) and can also be oxidized to *rect*-TiO₂ (reaction 11). The latter can be transformed into z -TiO_x and k -TiO_x upon heating in UHV (reaction 12). The z' -TiO_x phase can be directly obtained from the k -TiO_x by annealing in UHV (reaction 13).

Moreover, it has been found that the deposition of Ti onto the k -TiO_x and z -TiO_x films and subsequent postannealing does not lead to novel phases but provides some alternative routes

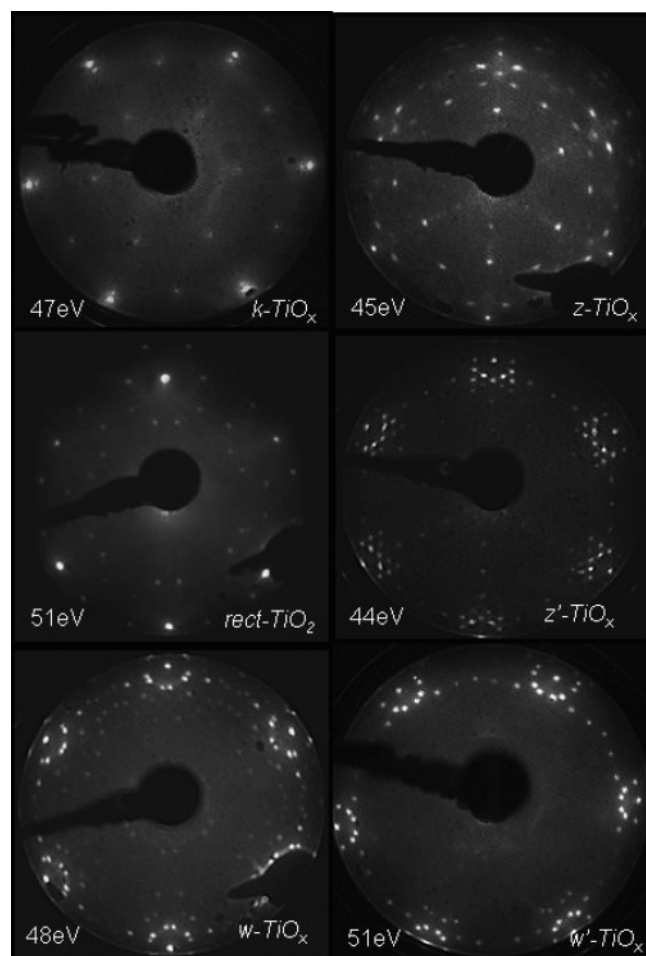
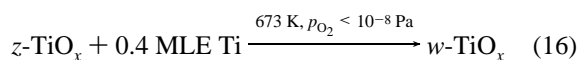
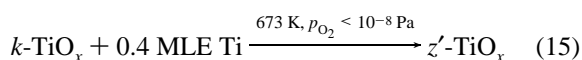
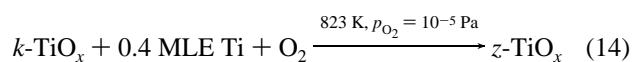


Figure 1. Summary of the LEED patterns of the observed TiO_x films on Pt(111).

for the preparation of $z\text{-TiO}_x$, $z'\text{-TiO}_x$, and $w\text{-TiO}_x$ according to the following equations:



Finally, it should be underlined that, by following preparative conditions different from the ones reported in eqs 1–6, LEED patterns of different phases could be somewhat superimposed, demonstrating that some of them can coexist. Actually, boundaries between them are clearly seen in some STM experiments (see below).

3.2. X-ray Photoemission and Photoelectron Diffraction.

The chemical characterization of the prepared nanostructures has been carried out by means of XPS.

Figure 2 shows the spin–orbit split Ti 2p core-level photoemission spectra of the observed TiO_x phases. In the upper part of the same figure, we also report, for comparison, the spectrum of a (2×2) Pt_3Ti surface alloy (prepared by deposition of one MLE of Ti in UHV and subsequently annealed at 823 K for 4 min),¹⁹ while in the lower part, we report the spectrum of a polycrystalline and stoichiometric TiO_2 film (approximately 80 Å thick). The latter is used as a reference for the fully oxidized

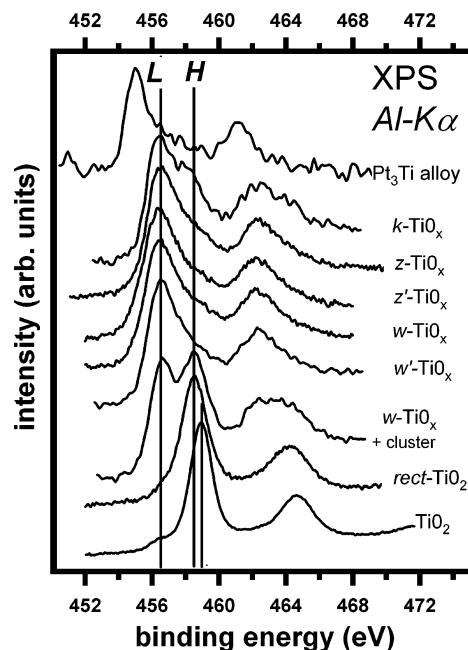


Figure 2. XPS spectra of TiO_x surface phases in the Ti 2p core level region. *L* and *H* correspond to the low and high binding energy peaks, respectively.

state of TiO_2 , i.e., the Ti^{4+} state. All spectra are normalized with respect to the intensities.

The TiO_x surface phases show two chemically shifted Ti 2p_{3/2} components with well-resolved BEs. In Figure 2, the lower BE component, centered at 456.4 eV, is labeled *L*, while the higher BE one, centered at 458.6 eV, is labeled *H*. The values are referenced to the Pt 4f_{7/2} photoemission peak and lie between those of the Pt_3Ti surface alloy (455 eV) and thick TiO_2 films (459 eV), but are clearly distinct from them.

The spectrum of *rect-TiO*₂ shows only the *H*-component. In all other phases, the *L*-component is the strongest feature in general, but we noticed the presence of a shoulder due to the *H*-component (well evident on the *k-TiO*_x), whose intensity may vary according to the different preparation procedure and sample history (see discussion below).

Although the relative binding energy position of the *L*- and *H*-components clearly indicates the higher oxidation state of the latter, we think that a straightforward assignment of each BE value to a well-defined oxidation state is not reliable. As pointed out recently in a review paper by Netzer et al.,²⁸ not only initial-state effects (chemical state related) but also final-state effects, such as screening and relaxation due to the metallic interface of the ultrathin oxide layer, have a significant effect in determining the BEs. Moreover, the whole concept of the formal metal oxidation state itself is probably meaningless when dealing with confined nanostructures in contact with a metallic surface. The Ti 2p BE assignment problem is well-illustrated in Figure 3, that provides a summary of published XPS data of the Ti 2p_{3/2} BEs for a broad range of different bulk samples, thick, thin, and ultrathin films on metal substrates. In these studies, the different BEs are assigned to Ti^{4+} , Ti^{3+} , Ti^{2+} , metallic, and alloy-like Ti^0 states (see references given in the caption of Figure 3). It is quite evident that the BE ranges associated to different oxidation states overlap. For all these reasons, we prefer to assign the XPS peaks to structural units rather than to oxidation states. One major structural issue regarding oxide films of nanoscale thickness is layer stacking determination. From the evidence provided by preliminary angle-scanned X-ray photoelectron diffraction (XPD) data, we

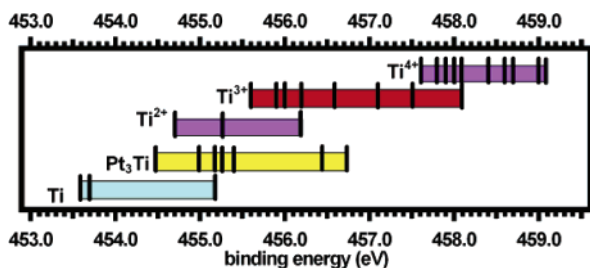


Figure 3. Binding energies of Ti $2p_{3/2}$ core levels from X-ray photoemission data. Values are taken from references as specified. Ti: refs 11, 19, 20. Pt_3Ti : refs 11, 19–22. Ti^{2+} : refs 16, 19, 23. Ti^{3+} : refs 10, 11, 16, 19, 24–27. Ti^{4+} : refs 10, 11, 19, 24–27.

propose that two-limit structural situations can be found in our TiO_x phases, Ti atoms sandwiched either in a Pt–Ti–O or O–Ti–O stacking, and consistently assign the H -component to the latter and the L -component to the former. The O–Ti–O stacking could exist in a ML phase, having an oxygen interface with Pt, or in a 3D island arrangement of the nanoscale layer. When the layer becomes thicker, the corresponding BE should shift toward the bulklike value.

Assuming this hypothesis, we can provide a rationale to the data reported in Figure 2. All the phases, except *rect*- TiO_2 , show the L -component, which means that Ti is most probably located at the interface with the substrate. In the case of *rect*- TiO_2 , the L -component is missing, suggesting that in this case there is an oxygen layer at the interface.

As already mentioned, strong support to this hypothesis comes from the analysis of preliminary XPD data. This technique is actually the best suited to provide the layer stacking sequence in ordered ultrathin films.²⁹ Such information can be derived in a straightforward way by exploiting the forward-scattering effect, which is at the basis of XPD when high kinetic energies of the photoelectrons are used.³⁰ Oscillations of the intensity can be observed when an ordered array of scatterers is interposed between an emitter and the detector. In other words, if the emitter is located at the outermost layer of an ordered ultrathin film, no intensity modulation of the corresponding XPS signal is observed. We want to outline that the azimuthal XPD curves of the z' - TiO_x , w - TiO_x , and w' - TiO_x phases show intensity oscillations only for the Ti 2p scans, while the corresponding O 1s curves are not modulated. On the contrary, the azimuthal curves for the *rect*- TiO_2 phase show intensity modulations both for Ti 2p and O 1s plots. This is only compatible with the presence of a Pt–Ti–O stacking for all phases except *rect*- TiO_2 . As an example of such different behavior, we report in Figure 4 XPD azimuthal Ti 2p and O 1s scans of the w - TiO_x and *rect*- TiO_2 phases for selected values of the polar angles. In the latter case, a Pt–O–Ti stacking sequence would explain the observed XPD pattern and the absence of the L -component in the XPS spectrum. This is also in accordance with the STM data reported in section 3.3.3.

As already pointed out, a H -type shoulder may be present in the spectra of the nanophases which are characterized by a predominant L -component. This effect is strongly dependent on the sample history and on subtle changes of the Ti dose and can be particularly pronounced for k - TiO_x , z - TiO_x , and w - TiO_x . In some cases, the intensity of the H -component may even exceed that of the L -component (as an example, we report in Figure 2 the spectrum labeled “ w - TiO_x + cluster”). The LEED pattern is however identical to the one where the H -component is absent. To solve this puzzling observation, STM has proven to be of crucial importance. In section 3.3.5 of this paper, we

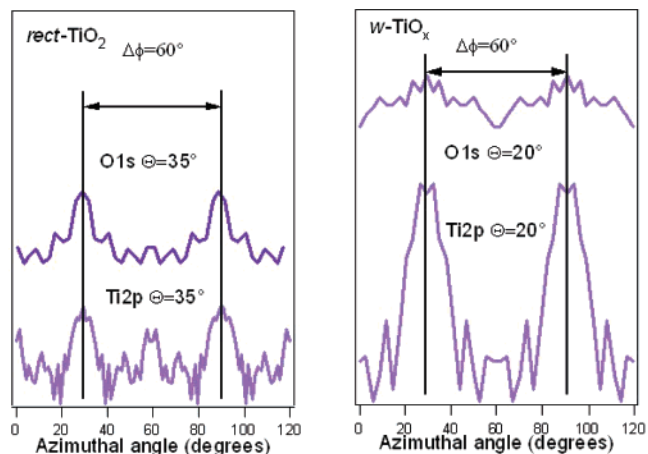


Figure 4. XPD azimuthal scans for Ti 2p and O 1s peaks of w - TiO_x and *rect*- TiO_2 at selected values of the polar angle Θ . The raw data were averaged according to surface symmetry to improve the statistics.

present in fact STM evidence for the growth of 3D TiO_2 clusters on some of the TiO_x phases. Moreover, we show the presence of wormlike structures on those parts of the Pt substrate that may remain uncovered during the preparation. These wormlike features show an apparent height which is larger than that of all the ordered phases except *rect*- TiO_2 . This is in agreement with an O–Ti–O stacking sequence. We conclude from these observations that the intensity variation of the H -component arises either from TiO_2 clusters or wormlike TiO_2 growth precursors, whose abundance may vary according to the sample preparation. Their surface density can be minimized by means of a well-optimized preparation.

All TiO_x phases reveal an O 1s peak whose BE is close to 530 eV with small shifts on the order of 0.3 eV. Moreover, in the phases where the Ti 2p L -component is predominant, the O 1s peak shows a pronounced tail in the higher BE side. On the contrary, for the *rect*- TiO_2 phase as well as in the TiO_2 thick film, the full width at half-maximum (fwhm) of the O 1s peak is narrower. This narrowing of the O 1s peak is consistent with the shift toward higher BE of the corresponding Ti 2p peak, that in turn is related to a more ionic character of the Ti–O bonding in the *rect*- TiO_2 phase and in the thick film. These Ti 2p peaks are themselves narrower and more symmetric than the ones measured from the predominantly L phases.

Finally, we remark that discussing stoichiometries for ordered ultrathin films directly from the intensities of the Ti 2p and O 1s components can also be misleading, because they are affected by structural effects, such as layer stacking, and by photoelectron diffraction phenomena. For this reason, we will refrain ourselves from drawing compositional information from the present XPS data.

3.3. Low-Energy Electron Diffraction and Scanning Tunneling Microscopy. In the following, we present and discuss the LEED patterns (Figure 1) and STM images of each phase summarized in Table 1. These results will be compared with similar data on related phases of other metal oxide systems, previously described in the literature.

A major point of general relevance is the actual assignment of the contrast in the STM images. This is always a hard undertaking to be assessed without a support from theoretical simulations of the STM images. In the following preliminary examination, we will assume that bright features at positive bias are to be associated with Ti localized empty states. However, a warning against such an overly simplistic interpretation of maxima in filled- or empty-state STM images in terms of

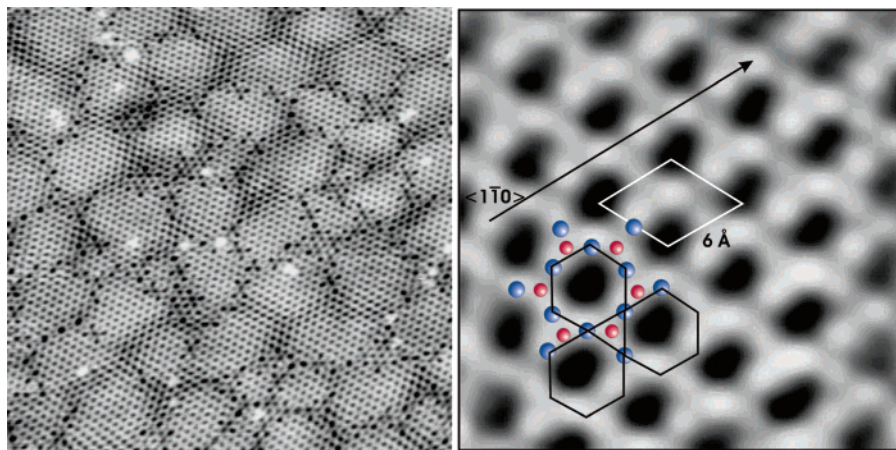


Figure 5. (a) Large-scale ($300 \times 300 \text{ \AA}^2$, $V = 1 \text{ V}$, $I = 1.0 \text{ nA}$) and (b) high-resolution ($30 \times 30 \text{ \AA}^2$, $V = -0.4 \text{ V}$, $I = 1.06 \text{ nA}$) STM constant-current images of the k - TiO_x phase.

individual atoms has to be made. In most cases, apart from but the simplest oxide structures, this approach is likely to be wrong if not supported by adequate theoretical assistance. There is enough experience with STM simulations that suggest that the states which are imaged are generally mixed and complex, and not single atoms. Often, entire building blocks of atoms give rise to a particular maximum in the STM image. Since theoretical simulations are not yet available for the observed phases, in the qualitative discussion that follows we will refrain from definitely assigning STM maxima or minima to individual atoms or vacancies. The assumption reported above (i.e., bright features at positive bias associated with Ti localized empty states) is only a first approximation, based on the current most accepted opinion of the contrast in STM images of TiO_x surfaces⁸ and is also in line with the conclusions of the extensive work done on ultrathin VO_x films on different single-crystalline metal surfaces, where the STM images have been analyzed on the basis of DFT calculations.^{1–6,31,32}

As already suggested in the discussion of the XPS data, 3D nanosized TiO_2 clusters on top of the surface-stabilized nanophases can be present if the Ti dose is higher than the amount needed to form the nanophases. In the following, we will describe some STM images (see section 3.3.5) where the presence of such nanoclusters is well evident. LEED experiments for deposits larger than 1.2 MLE do not show any new spots to be associated with diffraction from 3D nanoclusters, while the LEED patterns of the interface-stabilized nanophases are still observed. The low degree of structural order of the 3D clusters, as revealed by STM, can explain why their presence has not been detected by LEED. Actually, they rarely exhibit flat morphologies, and atomically resolved images have not been obtained.

3.3.1. Kagomé-Like TiO_x Phase (k - TiO_x). At low coverage of Ti (0.4 MLE) and after annealing the sample at the temperature of 673 K in an oxygen pressure of about 10^{-5} Pa (see Table 1 and eq 1), the k - TiO_x phase is obtained.

The LEED pattern, shown in Figure 1, indicates an incommensurate and hexagonal superstructure of the oxide. The evaluation of diffraction spots yields a $((2.15 \pm 0.05) \times (2.15 \pm 0.05))$ superstructure with respect to the Pt(111) substrate, which corresponds to an overlayer lattice constant equal to $6.0 \pm 0.1 \text{ \AA}$. Despite the mismatch with the Pt substrate, the unit cell of the oxide film is nevertheless rotationally aligned along the $\langle 1\bar{1}0 \rangle$ directions of Pt. According to XPS results, titanium is located at the interface with the platinum substrate.

Figure 5a reports a large-scale empty-states STM image of the k - TiO_x phase, taken at a positive bias. It appears that this phase forms a patched but clearly two-dimensional overlayer where a hexagonal motif is evident. The islands, which are about 60 \AA in size, display a long-range Moiré-like modulation in the STM image. The atomic rows continue over the boundaries of adjacent patches. Apart from the modulation of the contrast, a series of black spots are located at and closely around the patch boundaries. Very often, the black spots are arranged in X-shaped features. The apparent heights of the film with respect to the substrate range between 0.5 and 0.7 \AA , as determined from line profiles across the film–substrate boundary at various spots. The surprisingly low apparent height probably does not reflect the topography, rather being a result of the variation of the density-of-states at the boundary. Such an electronic effect, which causes similar low apparent heights, has been reported by Matsumoto et al. for $\text{TiO}_x/\text{Pt}(100)$ monolayers.^{10,11} The observed apparent height value suggests that the k -phase is composed by a Ti–O bilayer.

A high-resolution full-state STM image of the k - TiO_x phase, taken at a negative bias, is presented in Figure 5b. It shows a series of hexagonally arranged bright protrusions centered around dark sites. The dark spots are actually found at different bias values between -0.5 and $+1.2 \text{ V}$. The most likely explanation for this finding is that they are due to topography (a vacant pocket), and they reflect some kind of peculiar self-assembling of oxide building blocks.

The resulting structure shows a hexagonal surface mesh with a periodicity of approximately 6.0 \AA , in good agreement with the hexagonal 2.15×2.15 mesh seen by LEED. This value, multiplied by $1/2$, is in the range of O–O distances in titanium oxides that vary between 2.53 \AA (brookite) and 3.07 \AA (Ti_2O_3). The topology of the present structure is based on hexagons which are interconnected through their vertexes; this creates triangles defined by the connection points (see Figure 5b). Such a structure is called a kagomé lattice (it is the Japanese name for a woven bamboo basket which exhibits the same type of structure on a “macroscopic” scale). The increasing use of this expression in the solid-state related literature during the past few years is an indication of the relevance of such a lattice in the field of solid-state magnetism.^{17,18} The kagomé mesh is less densely packed in comparison with the common honeycomblike mesh, where hexagons share their edges.

One naïve interpretation of the image reported in Figure 5b could suggest that oxygen atoms are imaged in STM at a

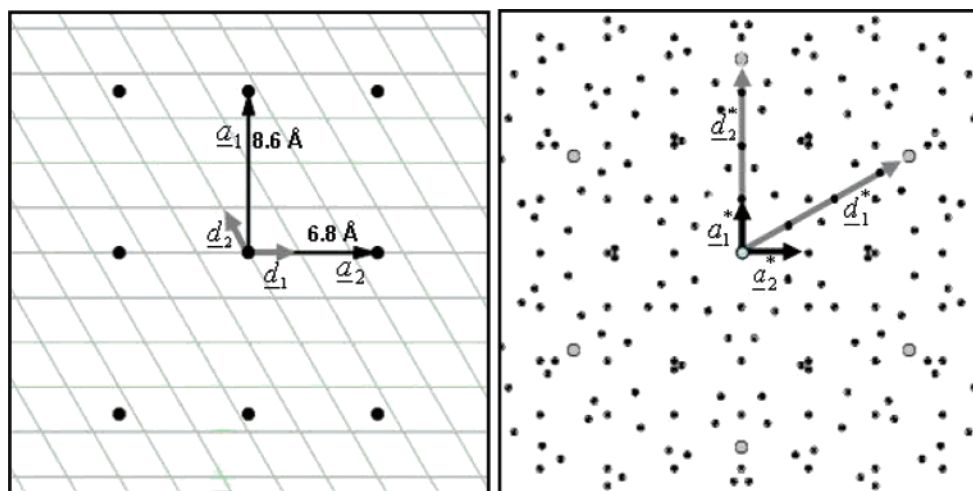


Figure 6. Details of the LEED pattern of *z*-TiO_x: real space (left) and reciprocal space (right). *a*₁ and *a*₂ denote the lattice vectors of the superstructure unit cell. Larger spots belong to the Pt(111) surface, and smaller ones to the three different domains of the overlayer.

negative bias voltage and that each bright spot corresponds to an oxygen atom. This would lead to the presence of three O atoms per unit cell, as indicated by blue circles in Figure 5b. One could therefore propose that the Ti atoms (red circles in Figure 5b), at the interface with the substrate, are located at the centers of the triangles. This structural model would imply a stoichiometry of two Ti and three O atoms per unit cell and hence a Ti₂O₃ composition for *k*-TiO_x. However, such an interpretation would mean tunneling into oxygen-filled states at a bias of -0.4 V, a rather unlikely hypothesis. DFT calculations are in progress to investigate the nature of the contrast in the reported image and also the factors which may favor the particular kagomé-like structure of *k*-TiO_x.

The kagomé pattern is also reported by Männig et al. for a one-monolayer TiO_x film on Ru(0001), when a flash annealing at 1000 K in 10^{-5} Pa is performed.¹² This coverage seems to correspond to 0.4 MLE, as used here. The authors state a $(6\sqrt{3} \times 6\sqrt{3})$ superstructure with a periodicity of 28.5 Å, based on their LEED data. The corresponding Moiré pattern, which they found in STM, arises from the superposition of the hexagonal Ru(0001) substrate lattice (surface lattice parameter 2.695 Å) and the oxide-related hexagonal net with a lattice parameter of 3.0 Å. However, the authors concluded from their data that the film is composed of an O–Ti–O layer where interfacial oxygen is bound to the Ru surface. The whole set of our experimental evidence on *k*-TiO_x/Pt(111), both from XPS and STM, is not in accordance with such a stacking and, in particular, excludes the interfacial oxygen from being present at the Pt(111) surface.

Similar to *k*-TiO_x/Pt(111), a kagomé-like mesh is reported for the system VO_x/Pd(111). Under comparable preparation conditions, a commensurate $(\sqrt{7} \times \sqrt{7})R$ 19.1° VO_x/Rh(111) phase is obtained by reactive evaporation of V on Rh(111) at similar coverages.^{5,6} The structural model of this particular VO_x phase, as derived by DFT calculations, is made up by pyramidal O₄V=O building blocks with V in the center, four O atoms on the basal plane, and one O atom at the apex of the pyramid. The apical O atom forms a double bond with the central V atom, and hence, the structure provides vanadyl species. The overall arrangement results in a V₃O₉ stoichiometry.

An evaluation of the step heights from line profiles of our STM data, complemented with XPS data, shows however that such a model cannot adequately describe the atomic arrangement of *k*-TiO_x. On the other hand, the hexagonal $p(2 \times 2)$ *s*-V₂O₃/Pd(111) phase^{1,4,33,34} (*s* = surface) bears some similarity with (2.15×2.15) *k*-TiO_x/Pt(111) in terms of the lattice type and

the alignment with the metal substrate. *s*-V₂O₃ exhibits two V atoms per unit cell that are located in fcc and hcp threefold hollow sites of the Pd(111) surface, and the O atoms are positioned above them in a bridging position. Apart from the fact that *s*-V₂O₃ is commensurate with Pd—in contrast to *k*-TiO_x/Pt(111) which is incommensurate—it also reveals a honeycomb lattice structure where the hexagons share their edges, a more compact lattice with respect to our kagomé mesh of *k*-TiO_x/Pt(111).

3.3.2. Zigzag-Like TiO_x Phases (*z*-TiO_x *z'*-TiO_x). At a nominal coverage of 0.8 MLE, we find two TiO_x phases, which both show zigzag-like structures in STM but reveal rather different LEED patterns. The *z*-TiO_x phase is best prepared by annealing at 823 K in 10^{-5} Pa oxygen (see eq 2).

The *z*-TiO_x phase shows a LEED pattern that can be assigned to an incommensurate superstructure with a rectangular unit cell of about $(6.8 \pm 0.1) \times (8.6 \pm 0.1)$ Å². The simulation of the diffraction spots is shown schematically in Figure 6, where both the real space and reciprocal space drawings are reported. Therein (as in all other successive figures), *d*₁ and *d*₂ denote the substrate lattice vectors, while *a*₁ and *a*₂ are the overlayer lattice vectors. The cell matrix notation of *z*-TiO_x is

$$\begin{bmatrix} 2.5 & 0 \\ 1.8 & 3.6 \end{bmatrix}$$

In the reciprocal space, the spots that arise from the three different domains (induced by the *P6mm* symmetry of the underlying (111) surface) of the overlayers are shown.

Figure 7a shows a large-scale STM image of the *z*-TiO_x phase. It forms a flat and continuous film which completely wets the platinum substrate. The wetting is actually so perfect that we did not find spots in STM at which the bare Pt substrate is visible. Therefore, the apparent height of the *z*-TiO_x phase with respect to the Pt(111) surface could not be determined. However, when *z*-TiO_x grows under slightly different experimental conditions, sometimes we found a few spots in the STM images where this phase coexists with *k*-TiO_x. An example is shown in the inset of Figure 7a. At these spots, line profiles can be determined across the boundary between the *z*- and *k*-TiO_x regions. The profiles show that the apparent height of *z*-TiO_x is higher by about 0.1–0.4 Å. The actual value depends on the applied bias voltage.

An atomically resolved image obtained at a low positive bias is reported in Figure 7b. It clearly reveals straight dark troughs with a periodicity of 8.6 Å perpendicular to their direction, a

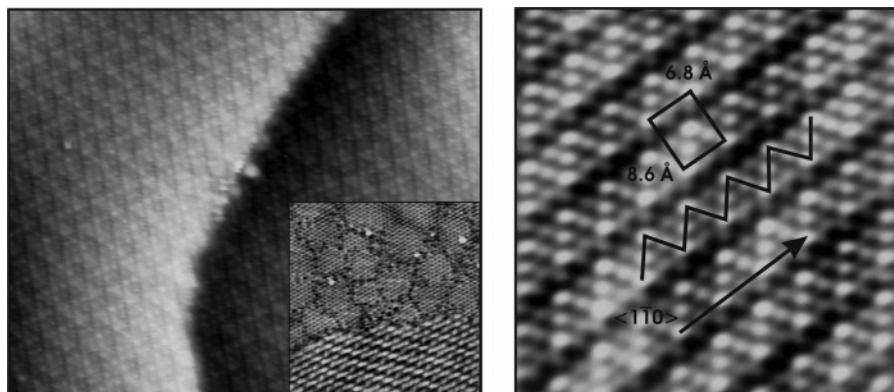


Figure 7. (a) Large-scale ($269 \times 226 \text{ \AA}^2$, $V = 0.6 \text{ V}$, $I = 1.0 \text{ nA}$) and (b) high-resolution ($60 \times 60 \text{ \AA}^2$; $V = 0.1 \text{ V}$, $I = 1.5 \text{ nA}$) STM constant-current images of the $z\text{-TiO}_x$ phase. The inset ($250 \times 250 \text{ \AA}^2$, $V = 0.2 \text{ V}$, $I = 1.1 \text{ nA}$) in (a) shows the boundary between $k\text{-TiO}_x$ and $z\text{-TiO}_x$.

zigzag-like motif, and a rectangular unit cell whose dimensions perfectly match the LEED values. The dark troughs do not show a significant bias dependence; hence, we conclude that they reflect the topography rather than the electronic contrast. They could be tentatively associated with rows of missing Ti atoms. The LEED data confirm that the *troughs* are aligned along the $\langle 1\bar{1}0 \rangle$ substrate directions. On the contrary, the zigzag motif shows a strong bias dependence. The zigzag feature consists of four bright spots per unit cell. The vertex protrusions are always brighter at any voltage, whereas the bumps between them appear brighter or darker as a function of the bias.

A striking similarity exists between $z\text{-TiO}_x/\text{Pt}(111)$ and the zigzag-like VO_x phase found on $\text{Pd}(111)$,^{1–4} an incommensurate structure which displays a rectangular unit cell of $6.9 \times 8.7 \text{ \AA}^2$. The lattice parameters are almost identical to those of $z\text{-TiO}_x$. Such a $\text{VO}_x/\text{Pd}(111)$ phase is observed at coverages in the 0.5 ML range and appears under these conditions as islands beside the honeycomblike surface- V_2O_3 phase. Their apparent heights range from 1.8 \AA to 3.0 \AA with respect to the $\text{Pd}(111)$ surface. The STM images of VO_x show a zigzag motif similar to $z\text{-TiO}_x$. On the basis of DFT calculations, the zigzag-like VO_x phase has been associated with a V_6O_{14} stoichiometry, and its structure has been shown to contain an O–V–O/ Pd stacking sequence.^{4,35}

A similar incommensurate TiO_x structure with a rectangular unit cell of $6.5 \times 8.7 \text{ \AA}^2$ is reported by Bennet et al.^{13,16} They observed it for TiO_x overlayers which are formed during the thermally activated encapsulation of $\text{Pd}(111)$ islands above 1200 K . The islands are grown on the (1×2) reconstructed TiO_2 – (110) surfaces. To rationalize the zigzag-like features imaged with STM, the authors first proposed an atomic model which consists of “rafts” of a centered rectangular O lattice ($4.7 \times 3.25 \text{ \AA}^2$ in size). They run along the $[001]$ direction of the $\text{Pd}(111)$ islands and are separated by troughs which are aligned along the $[001]$ direction. The model, which implies a TiO stoichiometry, suggests that Ti atoms bridge O atoms along $[001]$ and a Pd –O–Ti stacking sequence. The presence of a Ti-terminated surface, in particular, seems to be very unlikely, mostly because the phase is prepared under oxygen. In a recent paper, some of the previous authors give a completely different interpretation of the STM contrast, on the basis of the formation of a Pd –Ti surface alloy.¹³ However, they comment their interpretation as being “at least partially conjectural”.

Interestingly, the three systems $\text{TiO}_x/\text{Pt}(111)$, $\text{TiO}_x/\text{Pd}(111)/\text{TiO}_2$, and $\text{VO}_x/\text{Pd}(111)$, although composed of different metals, show very similar incommensurate rectangular unit cells. The structural models, reported in the literature for TiO_x and VO_x , are however distinct. Furthermore, they do not yield a consistent

description of $z\text{-TiO}_x$. A major discrepancy relates to the nature of the interface and the stacking sequence. Our XPS and XPD measurements are only consistent with interfacial titanium. Together with the STM observation, $z\text{-TiO}_x$ is likely composed by an O–Ti bilayer, exposing an oxygen termination.

A second zigzag-type phase, labeled $z'\text{-TiO}_x$, appears at the same coverage of 0.8 MLE but under reducing conditions (i.e., by annealing the sample in UHV at 673 K) (see eq 3).

The LEED pattern (Figure 8) can be assigned to a commensurate rectangular

$$\begin{bmatrix} 6 & 0 \\ 3 & 6 \end{bmatrix}$$

structure with a unit cell of $16.6 \times 14.4 \text{ \AA}^2$, as indicated by the sketch in Figure 6. Here, a_1 and a_2 refer to the short and long lattice vectors of the supercell, respectively.

Figure 9a shows the large-scale STM image of the $z'\text{-TiO}_x$ phase. Again, the layer grows as a continuous film on which parallel rows, spaced 14.4 \AA from each other, are clearly seen. The spacing is consistent with the LEED value of the short lattice constant. The observed rows appear always dark, independent from the applied bias voltage and its sign. This observation suggests that the troughs are topographic features, similar to the proposed Ti missing rows in $z\text{-TiO}_x$. In the STM image of $z'\text{-TiO}_x$, they show a somewhat wavy appearance as if the long-range order were not perfectly perpendicular to the troughs. In this sense, the disorder on this length scale is related to the LEED observation of this phase: it has been found to be difficult to obtain really sharp LEED spots in our STM setup (as they are easily obtained from $z\text{-TiO}_x$ and other phases), although in principle it is possible. For this reason, the STM images that are shown here for $z'\text{-TiO}_x$ might not reflect a fully ordered state. The high-resolution STM image in Figure 9b clearly reveals the zigzag-like motif, with a periodicity of 16.6 \AA along the troughs. This spacing, which perfectly matches the LEED result, is almost twice the value of the $z\text{-TiO}_x$ phase (8.6 \AA). If one goes along straight sections of the zigzag motif, the STM image also shows that they consist of five clearly resolvable bright protrusions and that the kinks of the zigzags are either V-shaped or W-shaped. Occasionally, we find that the straight sections of the zigzags contain one more additional bright spot, so that six atoms lie between the kinks. The varying distance, connected with this type of disorder, is likely responsible for the wavy character of the troughs on a larger length scale (Figure 9a).

Line profiles, taken at the boundaries of $z'\text{-TiO}_x$ and the substrate, indicate an apparent height of approximately 1 \AA with

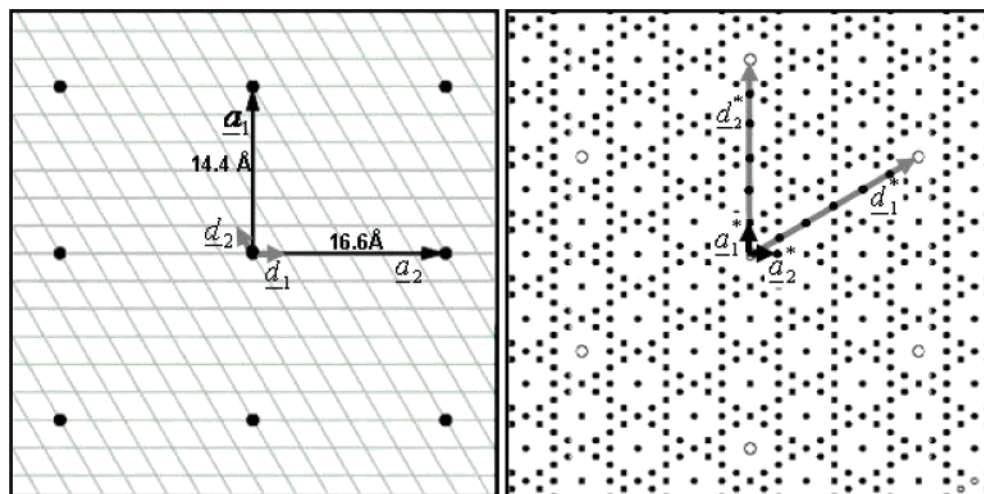


Figure 8. Details of the LEED pattern of z' - TiO_x : real space (left) and reciprocal space (right). a_1 and a_2 denote the lattice vectors of the superstructure unit cell. Larger spots belong to the Pt(111) surface, and smaller ones to the three different domains of the TiO_x overlayer.

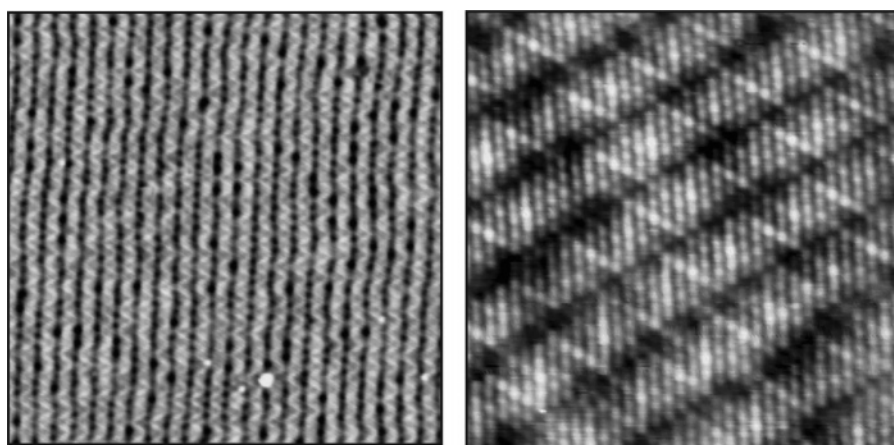


Figure 9. (a) Large-scale ($350 \times 350 \text{ Å}^2$, $V = 0.9 \text{ V}$, $I = 1.4 \text{ nA}$) and (b) high-resolution ($90 \times 90 \text{ Å}^2$; $V = 0.8 \text{ V}$, $I = 1.5 \text{ nA}$) STM constant-current images of the z' - TiO_x phase.

respect to the Pt(111) surface. This value is not significantly different from the height of the other zigzag-phase, z - TiO_x .

Such a zigzag-type phase has not been reported for the VO_x system. However, TiO_x overlayers that encapsulate Pt(111) islands (which are grown on $\text{TiO}_2(110)$) show indeed such a periodic zigzag-like structure, however with a slightly distorted rectangular unit cell. The STM images, reported by Dulub et al.,¹⁴ reveal a coincident oblique unit cell with dimensions of $13.85 \times 16.85 \text{ Å}^2$, i.e., somewhat different from our values of z' - TiO_x . No LEED data are available for this system, so symmetry and unit cell dimensions are not confirmed by a more accurate diffraction technique. Nevertheless, we will compare our z' - TiO_x phase with the corresponding structural model of Dulub's TiO_x phase that has been proposed by Jennison et al. on the basis of DFT calculations.¹⁵ These authors suggested that TiO_x is composed of a bilayer where Ti atoms occupy two different sites. One is located at the interface with the metal in either fcc or hcp hollow Pt sites. The second position, which does not provide an octahedral coordination for the Ti atoms, substitutes an oxygen atom at kink sites of the zigzags. Hence, these Ti atoms lie in the outermost layer, together with the oxygen atoms which occupy either bridge or hollow sites with respect to the interfacial Ti layer. This model offers an explanation for the zigzag motif: it arises from ordered misfit dislocations (the reader is referred to the structural model given in ref 15). Furthermore, the bright protrusions represent a topographical contrast, because they result from protruding

oxygen atoms. This explains the observed bias dependence of the kinks of the zigzags; at a negative bias, the kinks are brighter, since the tunneling current flows into the occupied states of the oxygen atoms.

Our interpretation of the STM data for the z' - TiO_x phase is in line with Jennison's model.¹⁵ It is also supported by our XPS findings, since the low binding energy Ti 2p peak confirms the presence of interfacial Ti atoms.

3.3.3. Rectangular Stoichiometric Phase (*rect*- TiO_2). The *rect*- TiO_2 phase is best obtained by deposition of 0.8 MLE or more of Ti with an annealing treatment at 973 K and $p_{\text{O}_2} = 10^{-4} \text{ Pa}$ (10 min) (see eq 4).

Its LEED pattern (Figure 1) can be attributed to an incommensurate

$$\begin{bmatrix} 1.16 & 0.18 \\ 0.58 & 1.56 \end{bmatrix}$$

overlayer, revealing a rectangular unit cell of $(3.8 \pm 0.1) \times (3.0 \pm 0.1) \text{ Å}^2$. The simulation of the diffraction spots is displayed in Figure 10. Again, the real space and reciprocal space drawings are shown in the left- and right-hand-side images, respectively. The unit cell axes are not aligned: they are rotated by an angle of 8.3° with respect to the principal directions of the Pt(111) substrate. In the real lattice of Figure 10, 8.3° corresponds to the angle between d_1 and the long lattice vector a_2 . The diagonal of the overlayer unit cell is aligned with

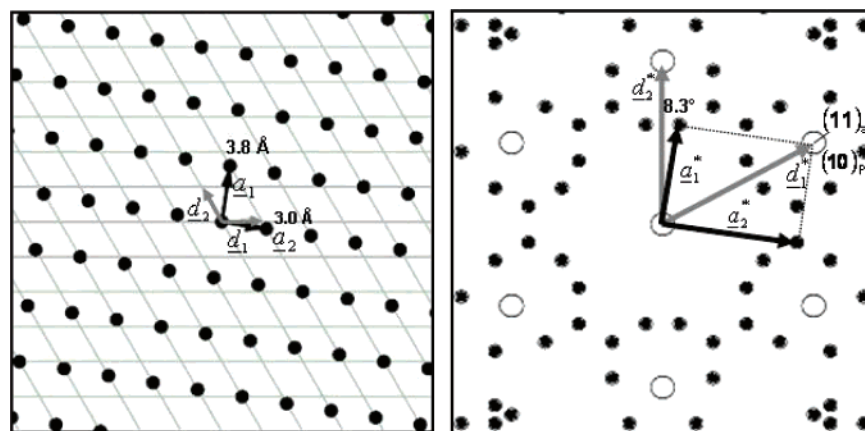


Figure 10. Details of the LEED pattern of *rect*-TiO₂: real space (left) and reciprocal space (right). a_1 and a_2 denote the lattice vectors of the superstructure unit cell. Larger spots belong to the Pt(111) surface, and smaller ones to the six different domains of the TiO₂ overlayer.

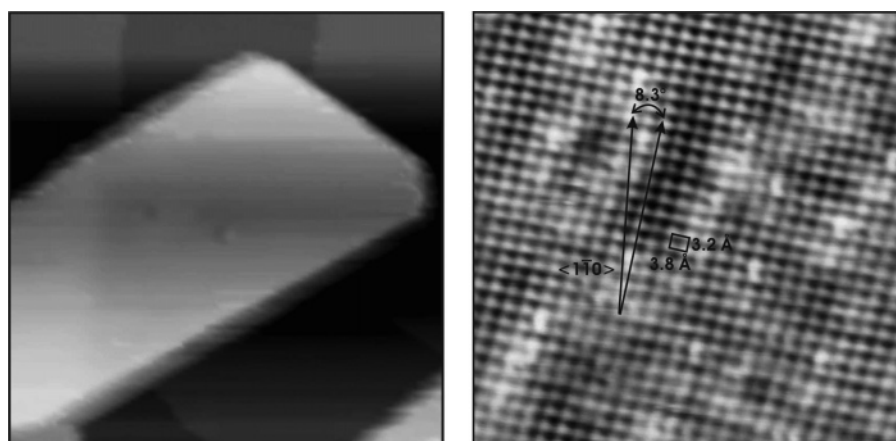


Figure 11. (a) Large-scale ($750 \times 750 \text{ \AA}^2$, $V = 1.3 \text{ V}$, $I = 1.5 \text{ nA}$) and (b) high-resolution ($90 \times 90 \text{ \AA}^2$, $V = 0.8 \text{ V}$, $I = 1.8 \text{ nA}$) STM constant-current images of the *rect*-TiO₂ phase.

the (10)_{Pt} direction, leading to a superposition of the (11)_a spot of the overlayer and the (10)_{Pt} spot of Pt.

Figure 11a reports a large-area STM image of the *rect*-TiO₂ phase where a rectangular island that expands over three different Pt(111) step edges is well evident. Large parts of the substrate are left uncovered. Line profiles show that the apparent height of *rect*-TiO₂ is approximately 2.5 \AA , i.e., significantly larger than the heights of the other TiO_x phases in this study. This can only be explained by a multilayer sequence rather than with a O–Ti bilayer. Figure 11b reveals the high-resolution STM image: the unit cell is marked by the small rectangle. Since a positive bias voltage is applied, the bright protrusions are tentatively attributed to the Ti atoms in an analogous manner as in the preceding sections. Comparison shows that the unit cell is in complete agreement with the LEED data.

The LEED pattern of *rect*-TiO₂ shows a close similarity with that of the *rect*-VO₂ phase reported by Surnev et al.^{2–4} This phase is formed at a nominal coverage of 1 ML of VO_x on Pd(111) and shows a LEED pattern compatible with a rectangular unit cell of $3.8 \times 3.2 \text{ \AA}^2$. The cell is rotated by an angle of 7.5° with respect to the [10 $\bar{1}$] direction of the Pd substrate. Kresse et al.³² report a structural model of *rect*-VO₂, based on DFT calculations, which was derived from the VO(110) surface, proposing oxygen terminations on both sides and octahedrally coordinated V atoms, with a stoichiometry of VO₂. This model implies a palladium–oxygen interface, with the occupation of the Pd on top and bridge positions by oxygen atoms. This is energetically favored over the occupation of Pd hollow sites

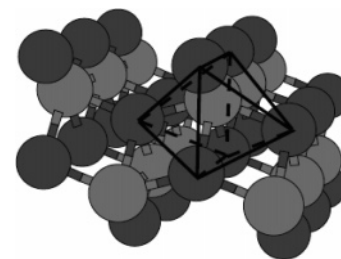


Figure 12. Structural model for *rect*-TiO₂/Pt(111) according to that of the *rect*-VO₂/Pd(111) (ref 32). Black and gray spheres represent oxygen and titanium atoms.

and represents a particular driving force, which explains the observed rotation of the *rect*-VO₂ phase (7.5°). By adopting this “misalignment”, the interfacial oxygen occupies only on top and bridge positions of the Pd surface.

Because of the striking similarity of the LEED patterns, the *rect*-VO₂ structure is a suitable candidate for modeling our *rect*-TiO₂ phase also (see Figure 12). Moreover, the Ti 2p_{3/2} core-level spectrum of this phase shows only the presence of the H-component, which fits nicely with the reported DFT model,³² where only one crystallographic site is occupied by the metal. This is also in tune with the XPD evidence reported in Figure 4, which shows intensity modulation for the O 1s peak in the corresponding azimuthal scan.

3.3.4. Wagon-Wheel-Like TiO_x Phases (w -TiO_x and w' -TiO_x). At a coverage of 1.2 MLE, we find two different TiO_x phases with distinct LEED patterns (displayed at the bottom of Figure

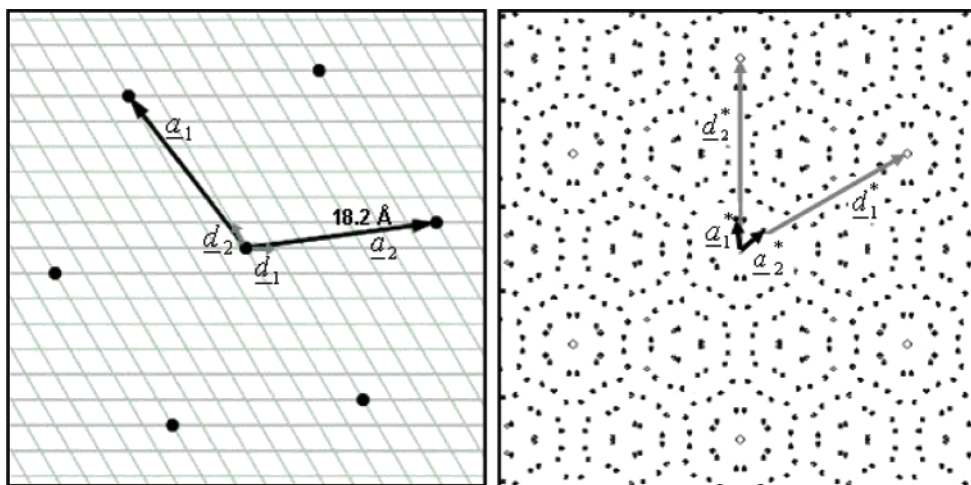


Figure 13. Details of the LEED pattern of *w*-TiO_x: real space (left) and reciprocal space (right). *a*₁ and *a*₂ denote the lattice vectors of the superstructure unit cell rotated by 7.6° with respect to the substrate. White spots belong to the Pt(111) surface, and black ones to the six different domains of the overlayer.

1), both revealing a commensurate and hexagonal superstructure. These films show a wagon-wheel-type appearance in STM and are correspondingly denoted as *w*-TiO_x and *w'*-TiO_x. The *w*-TiO_x phase is best obtained after a postannealing at 823 K and *p*_{O₂} = 10⁻⁵ Pa (5 min) (see eq 5), but we noticed that it can be obtained in a broad interval of temperature and annealing conditions.

The diffraction pattern is identical (but with sharper spots and better background) to the one previously observed by Boffa et al.⁹ and assigned to a hexagonal coincidence lattice, described by

$$\begin{bmatrix} 7 & 1 \\ -1 & 6 \end{bmatrix}$$

(or alternatively as (√43 × √43)*R* 7.6° in the Wood notation) with a unit vector of 18.2 Å. The simulation of the diffraction spots is displayed in Figure 13, where both the real space and reciprocal space drawings are reported.

Although our LEED pattern is similar to Boffa's, some experimental findings are different and are worth discussing in detail. According to Boffa et al.⁹ this phase exists in a larger coverage range between 1 and 5 MLs. There are of course differences in the determination of the coverage. However, clear XPD evidence is found that the (√43 × √43)*R* 7.6° LEED pattern is associated with a one-monolayer phase. It was shown in a previous study that TiO₂ clusters (that also may be called nanosized crystallites) grow on top of the (√43 × √43)*R* 7.6° phase also at larger coverages without perceivable differences of the LEED patterns.³⁶ Furthermore, the XPS results in Boffa's study differ from our data. We find a Ti 2p peak at a low binding energy of 456.4 eV, which is associated with interfacial Ti as in *k*-, *z*-, and *z'*-TiO_x. In contrast, Boffa et al. report stoichiometric TiO₂. This discrepancy may likely result from the circumstance that their XPS data refer to a situation where TiO₂ clusters and a *w*-TiO_x layer coexist. In that case, the Ti 2p *H*-component of the fully oxidized titanium in the clusters would obscure the interfacial *L*-component.

The *w'*-TiO_x phase is formed upon heating the *w*-TiO_x one at 723 K in UHV (4 min) (eq 7) or by deposition of 1.2 MLE of Ti, followed by annealing under identical conditions. The LEED pattern indicates a commensurate superstructure

$$\begin{bmatrix} 8 & 3 \\ -3 & 5 \end{bmatrix}$$

(or (7 × 7)*R* 21.8° in the Wood notation) and a hexagonal unit cell with a periodicity of 19.4 Å. The simulation of the diffraction spots is displayed in Figure 14. It is noteworthy that a (7 × 7)*R* 21.8° phase has been recently reported by Schoiswohl et al. for the reduced VO_x/Rh(111) system.^{5,6}

Both the *w*-TiO_x and *w'*-TiO_x phases give rise to a flat and continuous film which wets the entire Pt surface. Figure 15a reports a large-scale STM image of the *w*-TiO_x phase, which shows a hexagonal arrangement of black holes in perfect agreement with the cell dimensions determined from the LEED pattern. Each black hole is hexagonally surrounded by six bright protrusions. The high-resolution STM image obtained at a positive bias is reported in Figure 15b; it clearly shows atomic resolution. The overall appearance of the hexagonal dark spots, separated by 18.2 Å from each other, resembles a wagon wheel: a dark spot in the center, surrounded by the bright hexagons, represents the "hub" of the wagon wheel. A series of bright spokes that runs out from the centers, can be seen, too. The contrast is not bias-dependent. Using the mentioned contrast assumption, one could easily associate each bright spot to a Ti atom with a mean spacing of 3.3 ± 0.1 Å. It should be noted that Boffa et al.⁹ have already reported an STM image of such a phase, but without atomic resolution. In their images, they only resolve rows with a spacing of 3.5 ± 0.3 Å, and on this basis, they were not able to propose a satisfactory model.

Figure 16 shows an atomically resolved STM image of the *w'*-TiO_x phase. Again, the hexagonal unit cell is marked; the lattice vectors nicely match the LEED cell dimensions. Another wagon-wheel motif, different from the *w*-TiO_x, is present as well but with different dimensions and contrast. The "hub" of the wagon wheel is now created by a bright spot which is hexagonally surrounded by six other bright protrusions.

The apparent heights of *w*-TiO_x and *w'*-TiO_x are identical within the experimental error and almost identical to the values observed for the *z*-TiO_x and *z'*-TiO_x phases.

It has to be outlined that wagon-wheel structures are found for other oxide-on-metal systems where the oxides are grown as ultrathin films. Examples are TiO_x/Pd(111)/TiO₂(110)^{13,15} and (7 × 7)*R* 21.8° VO_x/Rh(111).^{5,6} Another example relates to metal-on-metal systems, an ultrathin Cr film on Pt(111).³⁷ Here, we will focus only on the structural model which has been recently discussed by Schoiswohl et al.⁶ for the (7 × 7)*R* 21.8° VO_x/Rh(111) phase. Using a DFT approach, they have derived a model from the VO(111) lattice. The wagon-wheel phase is

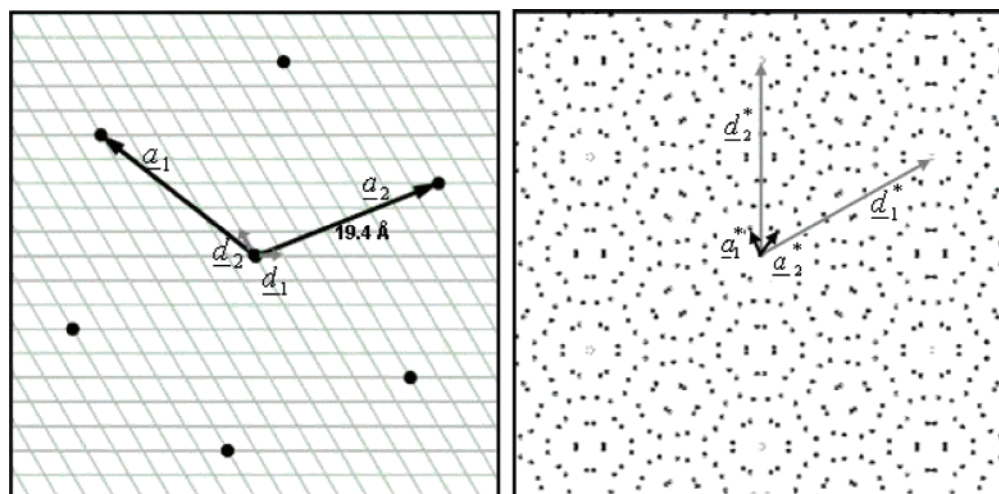


Figure 14. Details of the LEED pattern of w' -TiO_x: real space (left) and reciprocal space (right). a_1 and a_2 denote the lattice vectors of the superstructure unit cell rotated by 21.8° with respect to the substrate. White spots belong to the Pt(111) surface, and black ones to the six different domains of the overlayer.

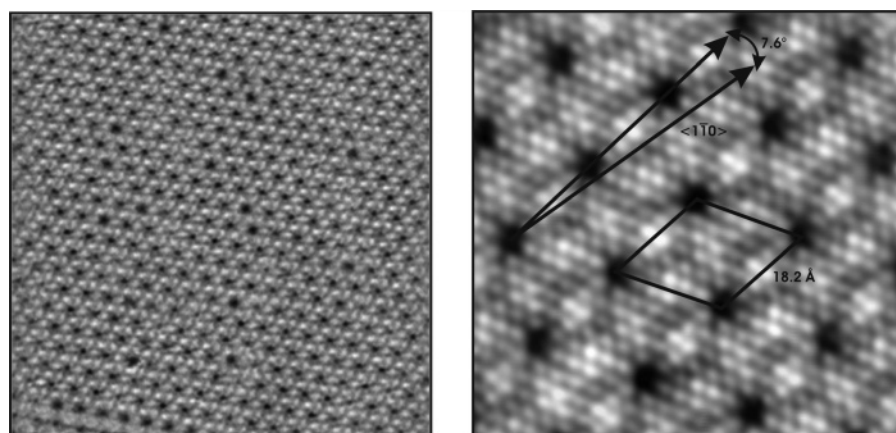


Figure 15. (a) Large-scale ($350 \times 350 \text{ \AA}^2$; $V = 1.0 \text{ V}$, $I = 0.6 \text{ nA}$) and (b) high-resolution ($75 \times 75 \text{ \AA}^2$; $V = 1.3 \text{ V}$, $I = 1.9 \text{ nA}$) STM constant-current images of the w -TiO_x phase.

composed of a V–O bilayer where V atoms are localized at the Rh interface. Hence, the phase is oxygen-terminated. The model suggests a VO stoichiometry.

Since our w' -TiO_x phase exhibits a $(7 \times 7)R 21.8^\circ$ mesh like the VO_x phase, the model of Schoiswohl et al. is certainly the first choice to examine our w' -TiO_x phase. It also fits our XPS and XPD data that we have collected from w -TiO_x and w' -TiO_x. The XPD intensity modulations are seen only for the Ti emitters, whereas the O 1s signal is almost not modulated. This is a strong indication that both phases consist of an O–Ti bilayer with Ti at the interface.

The large hexagonal unit cells can be interpreted as resulting from a Moiré pattern. The Moiré structure arises from the long-range coincidence of the Pt(111) lattice with the oxide superlattice. Figure 17a reports a schematic drawing of the hexagonal w -TiO_x phase with an atomic spacing of 3.26 \AA , placed on a hexagonal Pt(111) mesh with a periodicity of 2.77 \AA . The oxide lattice is rotated by 1.36° to match the Pt(111) net with the observed periodicity (18.2 \AA). This corresponds to a situation for which the $[7, 1]$ lattice vector of the Pt mesh is parallel to the $[6, 1]$ lattice vector of the overlayer, and hence, coincidence sites of the two lattices are created. They are indicated by black circles. This construction exactly reproduces the angle of 7.6° , by which the superstructure (i.e., the coincidence lattice) is rotated with respect to the main direction (e.g., $[1, 0]$) of the Pt(111) surface. This rotation angle is observed in LEED images.

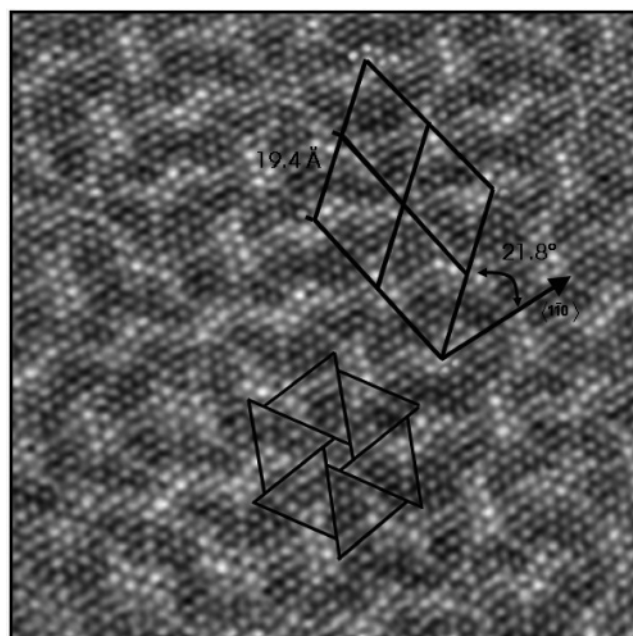


Figure 16. High-resolution ($126 \times 126 \text{ \AA}^2$; $V = 0.2 \text{ V}$, $I = 1.0 \text{ nA}$) STM constant-current image of the w' -TiO_x phase.

This construction also helps to understand the wagon-wheel motif in which the “light blue” Ti atoms in Figure 17a occupy

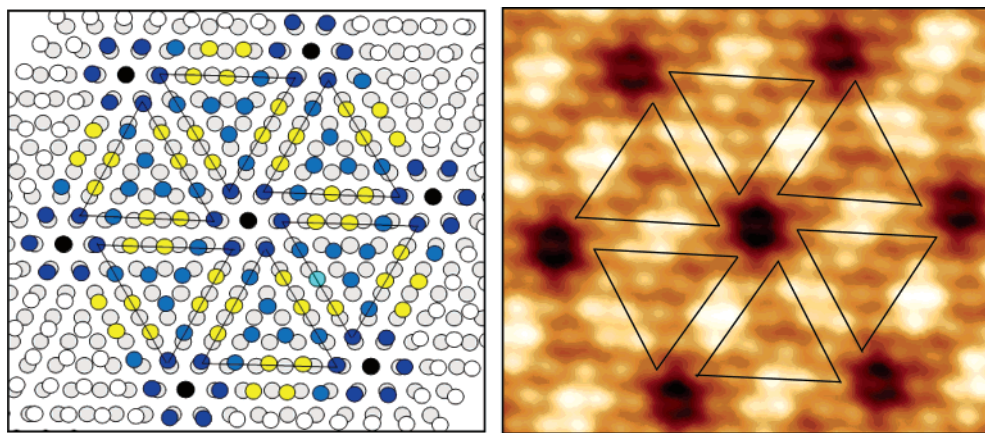


Figure 17. (a) Schematic drawing of the Moiré-like coincidence between the Pt(111) lattice and the w - TiO_x superlattice (color code: yellow = quasi-bridge; light blue = quasi-hollow; dark blue = quasi-top; black = coincidence or Ti vacancy, see text). (b) Corresponding atomically resolved STM image.

the quasi-hollow sites. The corresponding Ti atoms are located in the middle of the triangles in Figure 17b. The “yellow” Ti atoms on the side edges of the triangles (Figure 17a) bridge Pt atoms, and they therefore protrude more than the “light blue” ones; they appear brighter in the STM image (Figure 17b). The “dark-blue” atoms, which surround the coincidence site in the center, are quasi-on-top but appear nevertheless darker than the bridging atoms. Finally, the coincidence sites appear as black spots. Again, one important point concerns the contrast in the STM images. Since a positive bias is used, we tentatively associate the bright protrusions to interfacial Ti atoms. The comparison between the model and the image shows, however, that the contrast seems determined not only by the anticipated topographic height but also by electronic effects. This particularly holds for the “black holes” in the STM image of the w - TiO_x phase, whose nature remains unclear so far. They could be associated either to electronic effects due to the coincidence or to a Ti vacancy. Because of the observation that the w' - TiO_x structure with slightly larger dimensions is obtained after annealing w - TiO_x in UHV, we would prefer the Ti vacancy hypothesis. In other words, we suggest that the annealing in UHV could be effective in healing the Ti vacancies giving rise to a more reduced TiO_x phase.

In a similar fashion, one can construct the Moiré structure of the w' - TiO_x phase: one must take an oxide lattice parameter of 3.18 Å rotated by 3.5° in order to create the observed 19.4 Å periodicity of the $(7 \times 7)R$ 21.8° superstructure.

3.3.5. 3D Nanoclusters and Wormlike Growth Precursors. During the XPS investigations, we have noticed that the photoemission intensities of the H - and L -components of the Ti 2p levels may vary with respect to each other in a rather puzzling way. Spectra, normalized to the L -Ti 2p_{3/2} intensity, for some samples show a low intensity of the H -Ti 2p peaks and for others a high intensity, although the samples give identical diffraction spots in LEED. This fluctuation in peak intensity is mainly affected by slight variations of the initial Ti coverage and the growth conditions. Attempts to understand this observation in terms of varying stoichiometries and $\text{Ti}^{3+}/\text{Ti}^{4+}$ ratios failed entirely. With the help of the present STM experiments, however, a consistent explanation of the differences in the XPS spectra can be given. We find that fully oxidized titania is present on the surfaces of the bare Pt single crystal and/or the ordered TiO_x phases after the preparation. Titania either forms wormlike structures on the Pt surfaces or small clusters of nanosize dimensions which grow on the TiO_x phases. The wormlike structures, which are isolated or agglomerated,

indicate growth precursors and are found when part of the Pt surface remains uncovered, and hence, the transformation to a certain TiO_x phase has not been completed. The clusters seem to result from a local or overall excess of Ti during the formation of the ordered TiO_x phases. This is consistent with a competing growth of clusters and the ordered phase, the rates of which depend on temperatures and oxygen pressures. The cluster formation process is found to be facilitated by a high oxygen pressure in accordance with the +4 oxidation state of Ti in the clusters. However, clusters can also be seen on z' - and w' - TiO_x (which are produced under UHV conditions). A general observation is that the density of TiO_2 clusters becomes larger if Ti is further reactively deposited onto a TiO_x phase. On the other hand, the growth of ordered TiO_x phases above one monolayer thickness seems to be impossible (and in fact, ordered ultrathin films with larger thicknesses have not been found in this study), since the growth of clusters is favored. This is probably due to the intrinsically high stability of the Ti(IV) oxidation state.

Figure 18 shows three large-scale STM images where the wormlike, not ordered, features are clearly seen, grown on top of the Pt(111) surface and beside k - TiO_x (a), z' - TiO_x (b), and $rect$ - TiO_2 (c). The wormlike features show different apparent heights (0.8–1.1 Å) with respect to platinum and are always thicker than the ordered TiO_x phases, except $rect$ - TiO_2 . They are usually more densely packed close to the new phase boundaries (see Figure 18b) or to the rim of a Pt step edge (see Figure 18a). Figure 18c reveals them close to $rect$ - TiO_2 and over two different Pt terraces; the line profile is given in the inset. The image shows again that they are more densely packed close to the boundary between Pt(111) and the $rect$ - TiO_2 phase. It is therefore likely that they act as precursors for the growth of the ordered phases. The required surface mobility of such precursors is likely due to a Pt–O–Ti interface (which on the other hand explains the TiO_2 stoichiometry of the wormlike features).

Figure 19 shows two STM images of the TiO_2 clusters, grown on top of w - and w' - TiO_x . At initial stages of their growth, they appear as platelike islands. Despite their flat surfaces, atomic resolution has not been obtained with STM. Further dosing of Ti onto the surfaces and annealing (here, in oxygen for w - TiO_x , in UHV for w' - TiO_x), the clusters become more 3D-like and lose their regular shape. They do not yield diffraction spots in LEED, thus suggesting to be disordered. However, we have demonstrated in a previous XPD investigation that they exhibit a preferential azimuthal orientation with respect to the Pt(111)

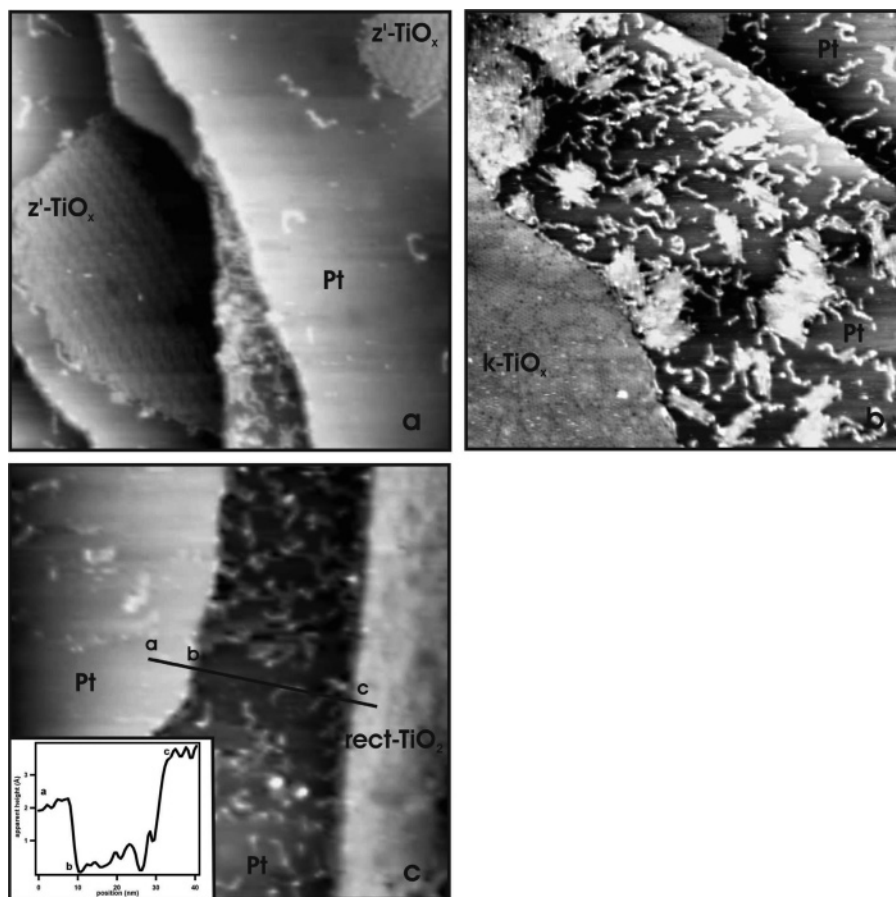


Figure 18. Large-scale ($600 \times 600 \text{ \AA}^2$) STM constant-current images showing the wormlike growth precursors beside to the (a) z' - TiO_x phase ($V = 0.8 \text{ V}$, $I = 0.8 \text{ nA}$), (b) k - TiO_x phase ($V = 0.2 \text{ V}$, $I = 0.7 \text{ nA}$), and (c) rect-TiO_2 phase. In the inset of (c), we report a line profile across a Pt(111) step edge and the boundary between the Pt(111) surface and the rect-TiO_2 phase.

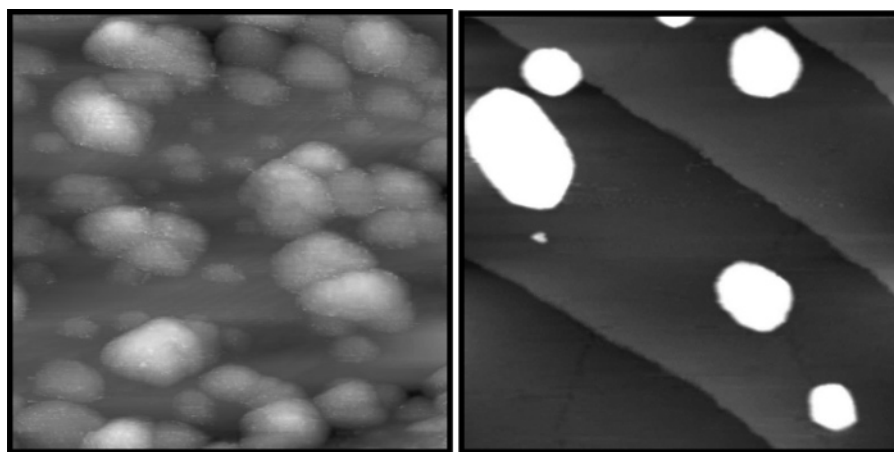


Figure 19. Large-scale topography of 3D clusters on w - TiO_x (high Ti dose) (left; $V = -1.0 \text{ V}$, $I = 0.3 \text{ nA}$, $1800 \times 1800 \text{ \AA}^2$) and on w' - TiO_x (low Ti dose) (right; $V = 1.0 \text{ V}$, $I = 1.2 \text{ nA}$, $1100 \times 1100 \text{ \AA}^2$).

surface.³⁶ This has been examined for the cluster-covered w - TiO_x phase in more detail. We have found a distinct XPD pattern of the Ti 2p and O 1s photoemission peaks, which can be explained by means of XPD simulations.³⁶ This confirms that the majority of the clusters are composed of rutile TiO_2 with the [100] direction parallel to the surface normal.

4. Conclusions

Considerable effort has been placed on finding reproducible preparation procedures of well-characterized ultrathin TiO_x overlayers on the Pt(111) surface and to explore the influence

of a variety of experimental factors, including coverage, annealing temperature and times, and oxygen partial pressure. Although this effort represents a kind of multiparameter search, we succeeded in finding those experimental conditions which determine the formation of ordered ultrathin, almost single-phase, and ordered titanium oxide films in the range of one monolayer. Transformations between the different phases have also been investigated and, if nonoptimized conditions are used, in some cases different phases can be coexistent. These phases have been characterized by means of XPS, LEED, and STM, and the results have been compared with literature data on

similar systems. Some preliminary XPD results were of high value in determining the thickness of the surface nanostructures and the nature of the atomic layer at the interface. Moreover, there is XPS evidence for the existence of stoichiometric TiO₂ at the surface. TiO₂ is present as clusters, either on top of the nano-TiO_x phases (e.g., when an excess of Ti is deposited) or beside them (as growth precursors when portions of the Pt(111) surface are left uncovered after an incomplete preparation).

The high-quality STM data reported here have allowed us to make a detailed comparison with some related systems, i.e., VO_x/Pd(111), VO_x/Rh(111), TiO_x/Ru(0001), and TiO_x/Pd(111)/TiO₂(110) and TiO_x/Pt(111)/TiO₂(110). This enables us to outline some general trends that may explain the nanostructures in terms of a simple chemical point-of-view. In the following, we will report some elementary speculations which could contribute to a better understanding of the mechanisms that control the growth of oxide nanostructures.

A thermodynamic picture of growth must take into account the surface and interface free energies of the metal substrate, the oxide/metal interface, and the oxide surface. More rigorous models would also include the kinetics of film growth and the involved lattice transformations. This is, however, beyond the scope of this report.

In agreement also with some argumentation reported by Netzer,²⁸ the habit of a peculiar interface-stabilized MO_x nanostructure over a metallic substrate (sub) is dictated by the following factors:

(a) the chemical properties of sub, in particular, with respect to its affinity toward oxygen, i.e., the stability of the sub–O bond.

(b) the tendency of sub to form alloys and surface alloys with the metal M of the MO_x overlayer, i.e., the stability of the sub–M bond.

(c) the chemical properties of the metal M with respect to oxidation states and its affinity toward oxygen.

(d) the mismatch between the overgrowing lattice and the substrate surface lattice.

Point (a) is particularly important during a reactive deposition in an oxygen background pressure. Actually, the incoming M atoms may hit either a bare sub surface or an oxygen chemisorption phase, according to the affinity of sub with oxygen. This will direct the formation of the film–substrate interface layer. From the sequence of bond energies of sub–O bonds, Ru > Rh > Pd > Pt, one may anticipate a similar trend for the presence of interfacial oxygen. The energies are in line with the standard heats of formation of metal oxides sub_aO_b.³⁸ Our study shows that interfacial oxygen is only present in *rect*-TiO₂ (obtained in extreme oxidation conditions), whereas the other phases reflect the low Pt–O bond energy.

Point (b) is more difficult to anticipate, but from an analysis of the literature data on surface alloys, it is apparent that Pt is suitable to form surface and bulk alloys. According to a comprehensive theoretical evaluation,³⁹ both Pt and Pd substrates have a similar tendency to form bulk alloys with Ti and V. This is also well-documented by the experimental observation of the easy thermally activated interdiffusion of Ti into Pt substrates. Actually, in accordance with the preferential Ti–Pt bond formation, all TiO_x phases (except *rect*-TiO₂) show interfacial titanium. This could suggest that commensurate Pt–Ti interfaces could be easily formed, which is somewhat in contradiction with the *k*-TiO_x and *z*-TiO_x incommensurate phases we have obtained. However, the following point (c) is also

relevant in determining the preference between a commensurate or an incommensurate phase.

To estimate the influence of the chemical properties of the metal M (point (c)), it is helpful to compare our results on TiO_x with VO_x. Vanadium, the right neighbor of Ti in the periodic table of elements, has one more electron in the valence shell with respect to Ti and consequently shows oxidation states up to V(+5) besides the +2, +3, and +4 states. The maximum oxidation state for Ti is Ti(+4). Moreover, it is well-known from inorganic chemistry that the vanadyl group V = O is more common than titanyl Ti = O, which is observed very rarely. By high-resolution electron energy loss (HREELS) experiments, it has been demonstrated by Netzer et al. that vanadyl-terminated VO_x surfaces are formed in VO_x nanostructures on Rh(111).⁶ A similar termination in TiO_x would be much less likely, even if recently some theoretical and experimental evidence for such a surface termination on the TiO₂(011) (2 × 1) surface has been reported.⁴⁰ In conclusion, further experiments using HREELS must be carried out to clarify such a point.

To go further with the comparison of Ti versus V, one has to take into account that Ti shows a greater affinity toward oxygen. The affinity is quantified by the standard heats of formation (TiO ≈ 500–550 kJ/mol; VO ≈ 400–450 kJ/mol). This might reflect the abundance of incommensurate structures we have found for TiO_x which are less common for VO_x phases. The driving force is then the stability of the overlayer rather than the overlayer/substrate interaction.

Finally, point (d), related to the strict geometrical requirements for an epitaxial growth, may in principle play a role in determining the observed nanostructures over the substrate hexagonal surface. However, we observe that the in-plane nearest-neighbor distances for the substrates herein considered are, respectively, Pt (2.77 Å), Pd (2.75 Å), Rh (2.69 Å), and Ru (2.69 Å). Their maximum difference amounts to 3%. Therefore, we assume that the overlayer/substrate lattice parameter matching plays only a minor role with respect to the chemical factors.

We are only at the beginning of a clear understanding of the driving forces and the underlying physical mechanisms that control the growth of oxide nanostructures. The growth of surface-stabilized TiO_x nanostructures seems to be controlled to a large extent by interaction with the platinum substrate. On the other hand, further experimental and theoretical work is needed to address those factors that control the particular structure of the TiO_x phases. A detailed description and analysis of the STM results of each phase, carried out with the aid of quantum mechanical calculations, will be the object of a forthcoming report.

Acknowledgment. This work has been funded by the European Community through the STRP project with the acronym NanoChemSens (Nanostructures for Chemical Sensors) within the SIXTH FRAMEWORK PROGRAMME (contract no. STRP 505895-1), by the Italian Ministry of Instruction, University and Research (MIUR) through the fund “Programs of national relevance” (PRIN-2003), project title “Defectivity and catalytic properties of ultrathin films and clusters”, by Research Program FISIR-MIUR “Nanosistemi inorganici ed ibridi per lo sviluppo e l’innovazione di celle a combustibile” and by the University of Padova, through the grant CP-DA038285. We would like to thank Prof. E. Tondello (University of Padova) for helpful discussions and Prof. F. Netzer (University of Graz) for a critical reading of the manuscript.

References and Notes

- (1) Surnev, S.; Vitali, L.; Ramsey, M. G.; Netzer, F. P.; Kresse, G.; Hafner, J. *Phys. Rev. B* **2000**, *61*, 13945.
- (2) Surnev, S.; Kresse, G.; Sock, M.; Ramsey, M. G.; Netzer, F. P. *Surf. Sci.* **2001**, *495*, 91.
- (3) Surnev, S.; Schoiswohl, J.; Kresse, G.; Ramsey, M. G.; Netzer, F. P. *Phys. Rev. Lett.* **2002**, *89*, 246101.
- (4) Surnev, S.; Ramsey, M. G.; Netzer, F. P. *Prog. Surf. Sci.* **2003**, *73*, 117.
- (5) Schoiswohl, J.; Sock, M.; Eck, S.; Surnev, S.; Ramsey, M. G.; Netzer, F. P.; Kresse, G. *Phys. Rev. B* **2004**, *69*, 155403.
- (6) Schoiswohl, J.; Surnev, S.; Sock, M.; Eck, S.; Ramsey, M. G.; Netzer, F. P.; Kresse, G. *Phys. Rev. B* **2005**, *71*, 165437.
- (7) Degen, S.; Becker, C.; Wandelt, K. *Faraday Discuss.* **2003**, *125*, 343.
- (8) Diebold, U. *Surf. Sci. Rep.* **2003**, *48*, 53.
- (9) Boffa, A. B.; Galloway, H. C.; Jakobs, P. W.; Benitez, J. J.; Batteas, J. D.; Salmeron, M.; Bell, A. T.; Somorjai, G. A. *Surf. Sci.* **1995**, *326*, 80.
- (10) Matsumoto, T.; Batzill, M.; Hsieh, S.; Koel, B. *Surf. Sci.* **2004**, *572*, 127.
- (11) Matsumoto, T.; Batzill, M.; Hsieh, S.; Koel, B. *Surf. Sci.* **2004**, *572*, 146.
- (12) Männig, A.; Zhao, Z.; Rosenthal, D.; Christmann, K.; Hoster, H.; Rauscher, H.; Behm, R. J. *Surf. Sci.* **2005**, *576*, 29.
- (13) Bowker, M.; Stone, P.; Morrall, P.; Smith, R.; Bennett, R.; Perkins, N.; Kvon, R.; Pang, C.; Fourre, E.; Hall, M. J. *Catal.* **2005**, *234*, 172.
- (14) Dulub, O.; Hebenstreit, W.; Diebold, U. *Phys. Rev. Lett.* **2000**, *84*, 3646.
- (15) Jennison, D. R.; Dulub, O.; Hebenstreit, W.; Diebold, U. *Surf. Sci.* **2001**, *492*, L677.
- (16) Bennett, R. A.; Pang, C. L.; Perkins, N.; Smith, R. D.; Morrall, P.; Kvon, R. I.; Bowker, M. J. *Phys. Chem. B* **2002**, *106*, 4688.
- (17) Honda, Z.; Katsumata, K.; Yamada, K. *J. Phys.: Condens. Matter* **2002**, *14*, L625.
- (18) Mekata, M. *Phys. Today* **2003** February, 12.
- (19) Bardi, U. *Catal. Lett.* **1990**, *5*, 81.
- (20) Hsieh, S.; Beck, D.; Matsumoto, T.; Koel, B. E. *Thin Solid Films* **2004**, *466*, 123.
- (21) Ringler, S.; Janin, E.; Boutonnet-Kizling, M.; Goethelid, M. *Appl. Surf. Sci.* **2000**, *162–163*, 190.
- (22) Chen, W.; Severin, L.; Goethelid, M.; Hammar, M.; Cameron, S.; Paul, J. *Phys. Rev. B* **1994**, *50*, 5620.
- (23) Robba, D. *Surf. Sci.* **1997**, *380*, 311.
- (24) Dwyer, D. F.; Cameron, S. D.; Gland, F. *Surf. Sci.* **1985**, *159*, 430.
- (25) Guo, Q.; Oh, W. S.; Goodman, D. W. *Surf. Sci.* **1999**, *437*, 49.
- (26) Kurtz, R. L.; Henrich, V. E. *Surf. Sci. Spectra* **1998**, *5*.
- (27) Liu, Z. M.; Vannice, M. A. *Surf. Sci.* **1996**, *350*, 45.
- (28) Netzer, F. P. *Surf. Rev. Lett.* **2002**, *9*, 1553.
- (29) Granozzi, G.; Samb, M. *Adv. Mater.* **1996**, *8*, 315.
- (30) Fadley, C. S. *Surf. Sci. Rep.* **1993**, *19*, 231.
- (31) Surnev, S.; Kresse, G.; Ramsey, M. G.; Netzer, F. P. *Phys. Rev. Lett.* **2001**, *87*, 86102.
- (32) Kresse, G.; Surnev, S.; Ramsey, M. G.; Netzer, F. P. *Surf. Sci.* **2001**, *492*, 329.
- (33) Klein, C.; Kresse, G.; Surnev, S.; Netzer, F. P.; Schmid, M.; Varga, P. *Phys. Rev. B* **2003**, *68*, 235416.
- (34) Samb, M.; Petukhov, M.; Domenichini, B.; Rizzi, G. A.; Surnev, S.; Kresse, G.; Netzer, F. P.; Granozzi, G. *Surf. Sci.* **2003**, *529*, L234.
- (35) Surnev, S.; Sock, M.; Kresse, G.; Andersen, J. N.; Ramsey, M. G.; Netzer, F. P. *J. Phys. Chem. B* **2003**, *107*, 4777.
- (36) Sedona, F.; Eusebio, M.; Rizzi, G. A.; Granozzi, G.; Ostermann, D.; Schierbaum, K. *Phys. Chem. Chem. Phys.* **2005**, *7*, 697.
- (37) Zhang, L.; van Ek, J.; Diebold, U. *Phys. Rev. B* **1999**, *59*, 5837.
- (38) Campbell, C. T. *Surf. Sci. Rep.* **1997**, *27*, 1.
- (39) Christensen, A.; Ruban, A. V.; Stoltze, P.; Jacobsen, K. W.; Skriver, H. L.; Nørskov, J. K.; Besenbacher, F. *Phys. Rev. B* **1997**, *56*, 5822.
- (40) Beck, T. J.; Klust, A.; Batzill, M.; Diebold, U.; Di Valentin, C.; Selloni, A. *Phys. Rev. Lett.* **2004**, *93*, 36104.